Bioorganic Chemistry 155 (2025) 108148

Contents lists available at ScienceDirect

Bioorganic Chemistry

journal homepage: www.elsevier.com/locate/bioorg

Triphenylphosphine-modified cyclometalated iridium^{III} complexes as mitochondria-targeting anticancer agents with enhanced selectivity

Hanxiu Fu, Shuli Wang, Yuwen Gong, Heqian Dong, Kangning Lai, Zhihao Yang, Chunyan Fan, Zhe Liu [1,*], Lihua Guo [*,2]

Key Laboratory of Life-Organic Analysis of Shandong Province, Key Laboratory of Green Natural Products and Pharmaceutical Intermediates in Colleges and Universities of Shandong Province, School of Chemistry and Chemical Engineering, Qufu Normal University, Qufu 273165 PR China

ARTICLE INFO

Keywords:
Cyclometalated complexes
Iridium
Triphenylphosphonium
Cytotoxicity
Target mitochondria

ABSTRACT

This study presents the development and evaluation of triphenylphosphine-modified cyclometalated iridium^{III} complexes as selective anticancer agents targeting mitochondria. By leveraging the mitochondrial localization capability of the triphenylphosphine group, these complexes displayed promising cytotoxicity in the micromolar range (3.12–7.24 μM) against A549 and HeLa cancer cells, these complexes exhibit significantly higher activity compared to their unmodified counterparts lacking the triphenylphosphine moiety. Moreover, they demonstrate improved specificity for cancer cells over normal cells, achieving selectivity index in the range of 5.46–14.83. Mechanistic studies confirmed that these complexes selectively target mitochondria rather than DNA, as shown by confocal microscopy and flow cytometry, where they accumulate to induce mitochondrial dysfunction. This disruption leads to mitochondrial membrane depolarization (MMP), elevated reactive oxygen species (ROS) levels, and activation of intrinsic apoptosis pathways. Furthermore, the complexes induce cell cycle arrest at the G_2/M phase and suppress the migration of A549 cells.

1. Introduction

Currently, significant progress has been made in the fields of tumor diagnosis and treatment, with the emergence of novel therapies such as targeted therapy, immunotherapy, and gene therapy, further advancing cancer treatment [1,2]. However, challenges remain in the realm of cancer therapy, including issues related to the systemic toxicity of small molecule drugs and the problem of drug resistance [3–5]. The development of multifunctional therapeutic agents has opened new possibilities for cancer diagnosis and treatment, particularly with the focus on anticancer drugs that integrate imaging and therapeutic functions within a single molecular framework [6–10]. Nevertheless, as of now, the development and research of multifunctional therapeutic agents still face several scientific challenges [11,12].

In the past decades, iridium complexes have shown remarkable anticancer properties and are emerging as a promising area of research in the advancement of metal-containing therapeutic agents for cancer treatment [13–15]. Iridium anticancer complexes can be mainly categorized into two structural classes: half-sandwich iridium complexes (Fig. 1, **I**) and cyclometalated iridium complexes (Fig. 1, **II**). Among these metal complexes, photoluminescent cyclometalated iridium^{III} compounds are particularly notable for their strong anticancer properties, which are mediated by strategies like targeting specific subcellular organelles and disrupting protein function [16–21]. Simultaneously, their exceptional optical characteristics, such as high quantum yields, significant Stokes shifts, adjustable emission wavelengths, superior photostability, and extended luminescence lifetimes, have established them as important assets in biological imaging and chemical sensing. These applications encompass tracking organelle activities and analyzing intracellular chemical species [22–26]. By contrast, half-sandwich iridium complexes generally lack these favorable photophysical properties, limiting their use in such applications. Therefore, cyclometalated iridium^{III} complexes hold great promise as innovative multifunctional theranostic agents, seamlessly integrating imaging capabilities with anticancer activity into a single platform [16,27–29].

Mitochondria, a central hub for cell signaling, are vital organelles

---

* Corresponding authors.

E-mail addresses: liuzheqd@163.com (Z. Liu), guolihua@qfnu.edu.cn (L. Guo).

[1] ORCID: 0000-0001-5796-4335.

[2] ORCID: 0000-0002-0842-9958.

https://doi.org/10.1016/j.bioorg.2025.108148
Received 18 November 2024; Received in revised form 29 December 2024; Accepted 6 January 2025

responsible for energy generation and are essential in regulating biological processes, including apoptosis, calcium ion balance, and cellular metabolism [26,30,31]. Dysfunction of mitochondria is closely associated with various diseases, including cancer and neurodegenerative disorders [32]. Tumor cells and normal cells exhibit significant in both the structure and function of their mitochondria. Due to extensive mutations, tumor cells have a more fragile redox balance and genomic instability, making them more susceptible to mitochondrial damage [33]. Mitochondrial-targeted compounds have emerged as a promising strategy for combating chemotherapy-resistant cancer cells, driving increased interest in the development of luminescent therapeutic agents designed to target mitochondria [34]. Triphenylphosphine (TPP) is a widely utilized lipophilic cationic ligand that targets mitochondria [35]. Its structure features a positively charged phosphorus atom bonded to three benzene rings, giving it high lipid solubility. The arrangement of the phenyl groups shields the phosphorus from solubilization. Additionally, the positive charge on the phosphorus can be delocalized across the three benzene rings, which, along with the negative membrane potential of mitochondria, enhances TPP's ability to traverse lipid bilayers and selectively accumulate within mitochondria [35,36].

The methyl-triphenylphosphonium (TPP) cation, as the first organic small molecule of its type, demonstrates selective accumulation in mammalian cell mitochondria, driven by their high membrane potential (Fig. 1, **III**) [37]. Mitochondrial drug delivery has been enhanced by tethering bioactive molecules to TPP via alkyl chains or other covalent linkages, broadening its utility in mitochondrial research (Fig. 1, **IV**) [38–40]. Despite limited applications, TPP and its derivatives have been explored as scaffolds or chelating ligands in designing metal-based agents with anticancer and antimicrobial properties [40–43]. For instance, conjugation of cisplatin with TPP (Fig. 1, **V** and **VI**) redirects its action toward mitochondria rather than nuclear DNA, enabling integration into the mitochondrial genome and modulation of cellular processes [42,43]. Thus, this mitochondrial targeting strategy has been shown to effectively overcome cisplatin resistance [42]. Notably, previous studies have demonstrated that attaching specific groups, such as chloromethyl on bipyridine (bpy) in cyclometalated iridium^{III} complexes, can facilitate mitochondrial targeting by reacting with thiol groups in mitochondrial proteins via nucleophilic substitution (Fig. 1, **VII**) [16]. Inspired by these encouraging results, we sought to develop new anticancer complexes based on platinum group metals, by coupling with the triphenylphosphonium (PPh^{3+}) moiety, aiming to combine the advantages of mitochondria-targeting ability of PPh^{3+} moiety and photoluminescent properties of cyclometalated iridium^{III} complexes (Scheme 1). Herein, we synthesized a series of triphenylphosphine-modified photoluminescent cyclometalated iridium^{III} complexes specifically designed for mitochondrial targeting. This targeted design enhances mitochondrial accumulation and induces apoptosis in cancer cells, resulting in high anticancer activity and improved selectivity for cancer cells over normal cells. Additionally, the photoluminescent properties of these complexes enable real-time tracking within cells, offering valuable capabilities for biological imaging. This multifunctional approach effectively addresses key limitations of existing iridium-based anticancer agents, such as limited selectivity, unclear targeting, and ambiguous mechanisms of action.

2. Results and discussion

2.1. Synthesis and characterizations

Cyclometalated iridium^{III} precursors **D1**–**D5** were synthesized using reported methods [44,45]. The phenanthroline-based NˆN chelating ligand **L1** was prepared with a moderate yield through the reaction of (4-(4-formylphenoxy)butyl) triphenylphosphonium bromide with phenanthroline-dione and excess NH$_4$OAc, following a modified protocol (Scheme 1a). **L2**, which did not contain triphenylphosphine moiety, was also prepared following literature method [41]. The triphenylphosphine-modified complexes **Ir1**–**Ir5** were synthesized in 43–61 % yields by reacting the metal precursors **D1**–**D5** with the

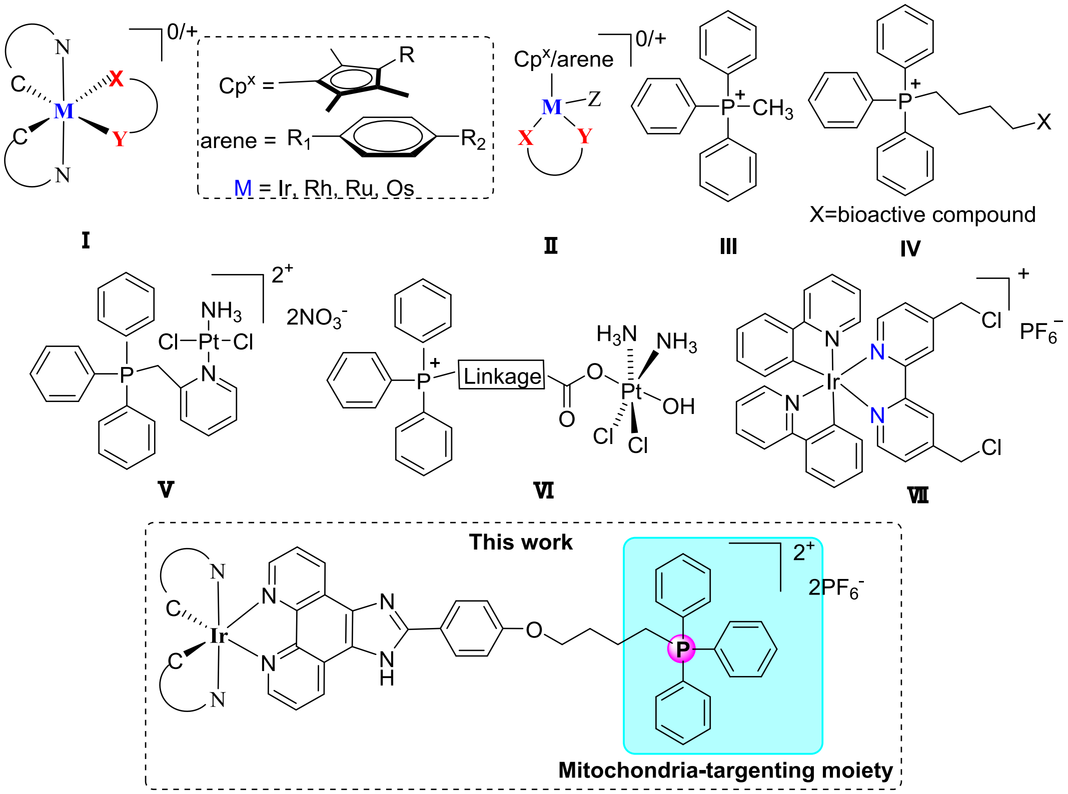

Fig. 1. The cyclometalated complexes and half-sandwich complexes, known triphenylphosphine-containing compounds and our current work.

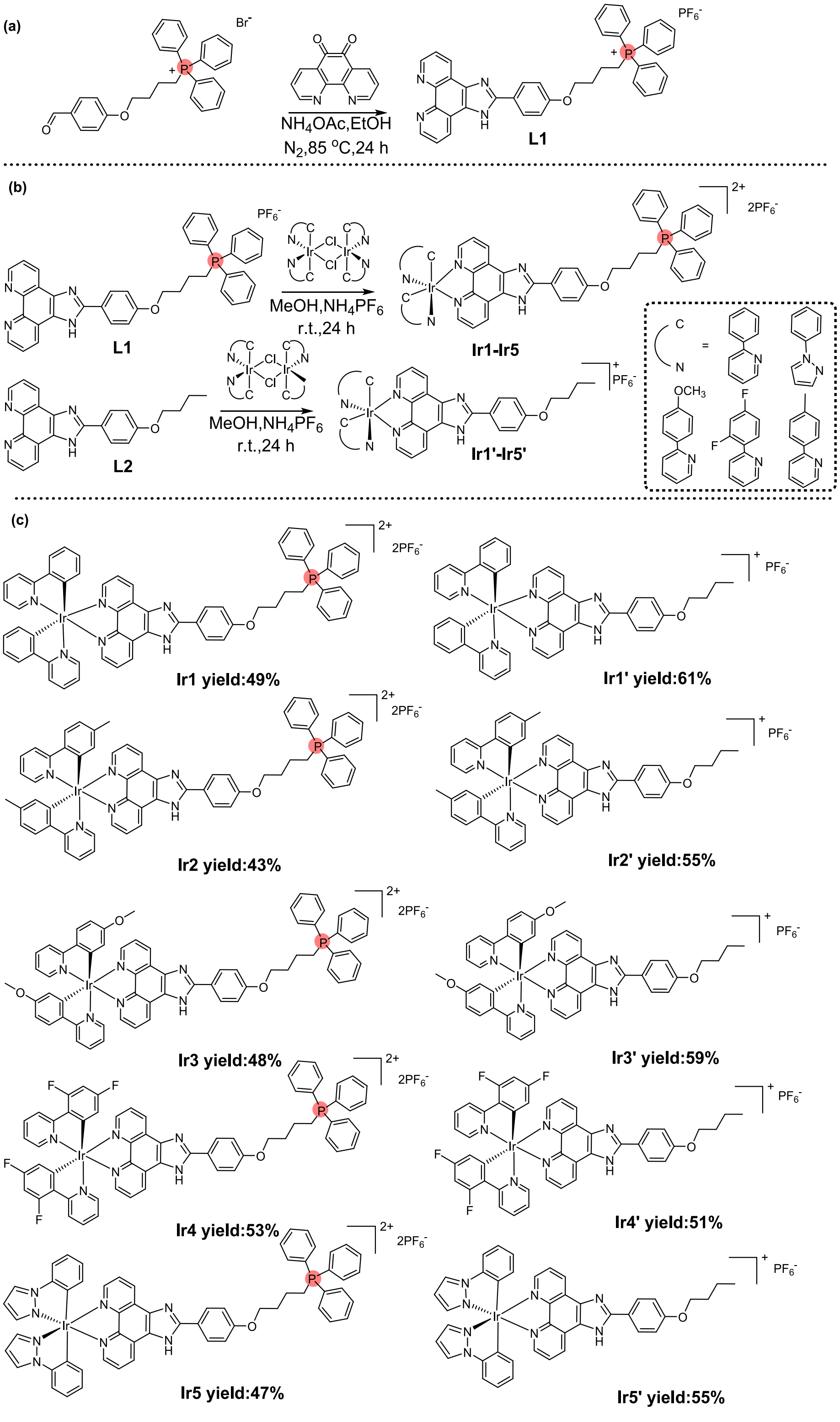

Scheme 1. Preparation of ligands **L1** (a), synthesis of cyclometalated iridium^{III} complexes (b), and the detailed structures of **Ir1–Ir5** and **Ir1'–Ir5'** (c).

corresponding ligands in a solution of CH_2Cl_2 and CH_3OH (v/v = 1:1) (Scheme 1b). For comparison, the corresponding complexes **Ir1'–Ir5'** which lack the triphenylphosphine moiety, were similarly prepared (Scheme 1b). The detailed structures of **Ir1–Ir5** and **Ir1'–Ir5'** are also depicted in Scheme 1c. The formation of the desired complexes was thoroughly confirmed using ^1H, ^{13}C, ^{31}P and ^{19}F NMR (Figs. S1–S32 in Supplementary materials), elemental analysis and mass spectroscopy (Figs. S33–S42 in Supplementary materials). ^1H NMR spectra showed that molar equivalents of bound arene per mole of ligand were detected in these complexes, indicating coordination between the ligands and the metal ions. ^{31}P NMR analysis distinctly shows that in the complexes **Ir1–Ir5,** the triphenylphosphine (PPh^{3+}) moiety and the PF_6^- counteranion produce a singlet and a septet at approximately δ24 ppm and −140 ppm, respectively (Figs. 2, S3, S6, S9, S12 and S16). Conversely, only a septet, corresponding to the PF_6^- counteranion, was observed in the complexes **Ir1'**–**Ir5'** without triphenylphosphine moiety (Figs. 2, S19, S22, S25, S28 and S32). The ^{19}F NMR analysis clearly showed that the fluoro complexes **Ir4** and **Ir4'** display two doublets at approximately δ −107 ppm corresponding to the fluorine substituents on the phenylpyridine(ppy) ligand, while the PF_6^- counteranion produces two singlets at around δ −70 ppm (Figs. S13 and S29).

Multiple attempts to grow single crystals of the triphenylphosphine-containing complexes were unsuccessful. However, Single crystals of the triphenylphosphine-free control complex **Ir4'** were successfully prepared by allowing *n*-hexane to slowly diffuse into its CH_2Cl_2 solution. The structure of **Ir4'** was then determined and validated using X-ray crystallographic analysis (Fig. 3 and Table S1). In the **Ir4'** complex, the cationic iridium^{III} center shows coordination with the *N,N*-chelating ligand, resulting in a distorted octahedral configuration around the metal center. The coordination around the metal center in the two phenylpyridine (ppy) ligands exhibits a mutually cis C,C and trans N,N configuration. The Ir–N bond lengths in 1,10-phenanthroline-based ligand (Ir1–N1:2.119 Å and Ir1–N2: 2.132 Å) are slightly longer compared to those in the ppy ligands (Ir1–N5: 2.041 Å and Ir1–N6: 2.049 Å).

2.2. Absorption and emission spectroscopy

The UV–vis spectra of **Ir1**–**Ir5** and **Ir1'**–**Ir5'** in methanol solutions at 37 °C are presented in Fig. 4a. These iridium^{III} complexes all show strong absorption bands in the high-energy region (less than 350 nm), which are associated with spin-allowed π-π^* electronic transitions of the ligands. Broad and featureless absorption bands in the 350–450 nm range are attributed to metal-to-ligand charge transfer transitions (MLCT) [46,47]. Additionally, lower-energy bands appearing in the visible region (>450 nm) are ascribed to a combination of singlet and triplet MLCT transitions (^{1}MLCT and ^{3}MLCT). The absorption characteristics of these complexes resemble those of cyclometalated iridium^{III} complexes reported in earlier studies [44,48–50].

Upon excitation at a wavelength of $\lambda_{ex} = 388$ nm, the **Ir1**–**Ir5** and **Ir1'**–**Ir5'** complexes exhibit emission wavelengths (λ_{em}) that span from 540 nm to 611 nm (Fig. 4b: **Ir1** (598 nm), **Ir2** (603 nm), **Ir3** (609 nm), **Ir4** (611 nm), **Ir5** (600 nm), **Ir1'** (601 nm), **Ir2'** (550 nm), **Ir3'** (540 nm), **Ir4'** (599 nm), and **Ir5'** (595 nm)) when measured in methanol at 37 °C. Consistent with their absorption spectra, substitutions on the ligands have no obvious impact on the emission spectra. The relative emission quantum yields (Φ) of the iridium^{III} complexes in an ethanol solution, determined using fluorescein as a standard, range narrowly from 0.390 to 0.527 (**Ir1**: 0.491, **Ir2**: 0.489, **Ir3**: 0.527, Ir4: 0.512, **Ir5**: 0.432, **Ir1'**: 0.453, **Ir2'**: 0.390, **Ir3'**: 0.417, **Ir4'**: 0.464, **Ir5'**: 0.437), demonstrating a lack of sensitivity to changes in the complex structure. Furthermore, the average fluorescence lifetimes of the **Ir1–Ir5** complexes were also measured, with values ranging from 219.52 to 319.19 ns (Fig. S43, **Ir1**: 258.68 ns, **Ir2**: 219.52 ns, **Ir3**: 250.08 ns, **Ir4**: 241.19 ns, **Ir5**: 319.19 ns), indicating that these complexes exhibit fluorescence. The photoluminescent properties of these complexes facilitate bio-imaging analysis, enabling exploration of their mechanisms of action. Thus, these complexes are anticipated to serve as versatile theranostic platforms, combining anticancer activities with imaging functionalities in a single compound.

2.3. Solution stability

The stability of **Ir1**–**Ir5** and **Ir1'**–**Ir5'** was evaluated in a containing of 20 % DMSO and 80 % PBS (obtained using H_2O, pH ≈ 7.4,) at 37 °C over a 24-hour period using UV–vis spectroscopy. The absorption spectra showed minimal changes, indicating that these iridium^{III} complexes were stable in dilute aqueous solutions (Fig. S44). Additional stability tests were performed using ^1H NMR spectroscopy under similar conditions (80 % DMSO-d_6 and 20 % PBS, pH ≈ 7.4, obtained using D_2O) at 37 °C. The ^1H NMR spectra revealed no new peaks for **Ir1–Ir5** and **Ir1'-Ir5'** over the same time period (Figs. S45-S54), confirming that the complexes retained their structural integrity without dissociation. Overall, their stability was consistent with that of previously reported *N*,*N*-chelating cyclometalated iridium^{III} complexes, [49,52] supporting

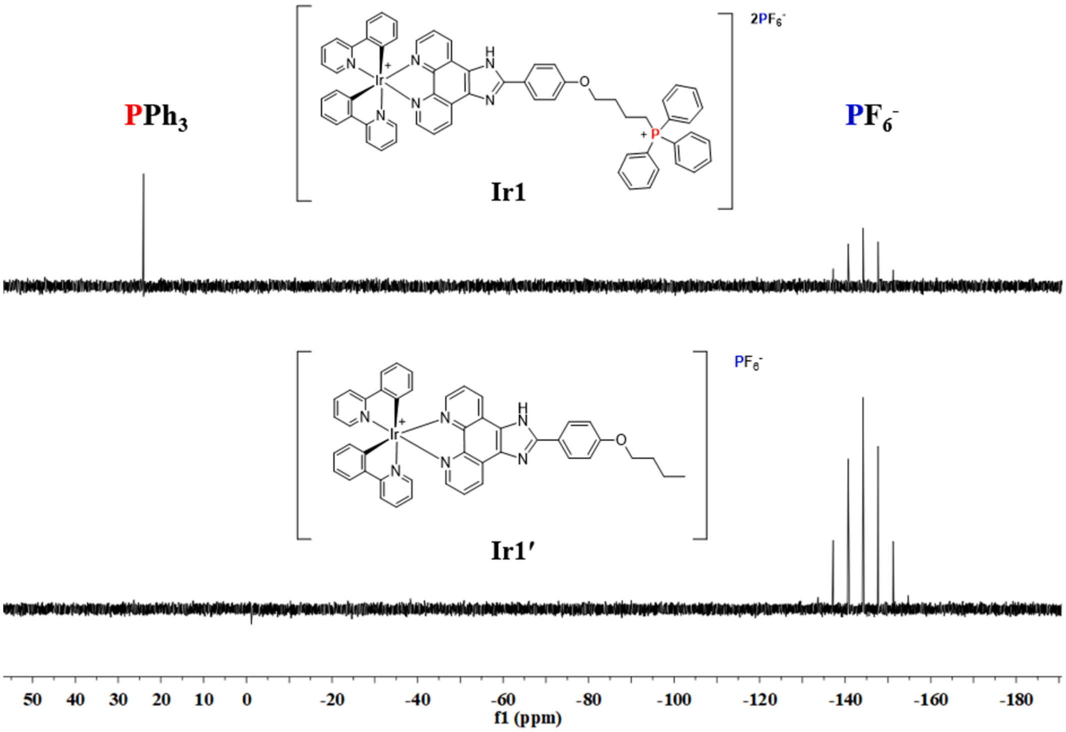

Fig. 2. ^{31}P NMR spectrum of the phosphorus complexes **Ir1** and **Ir1'**.

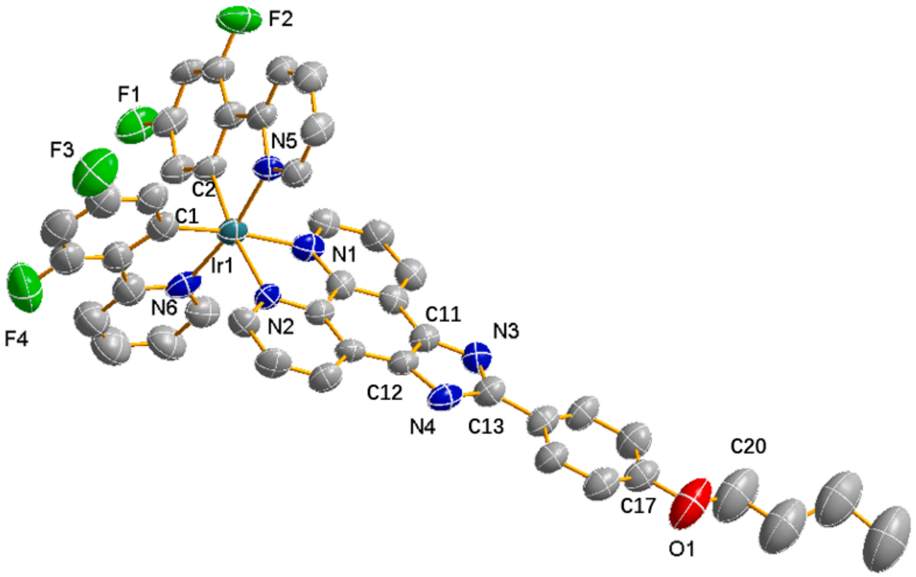

Fig. 3. X-ray crystal structure of complex **Ir4'**, with thermal ellipsoids shown at 50% probability. For clarity, hydrogen atoms and the anion have been excluded from the illustration.

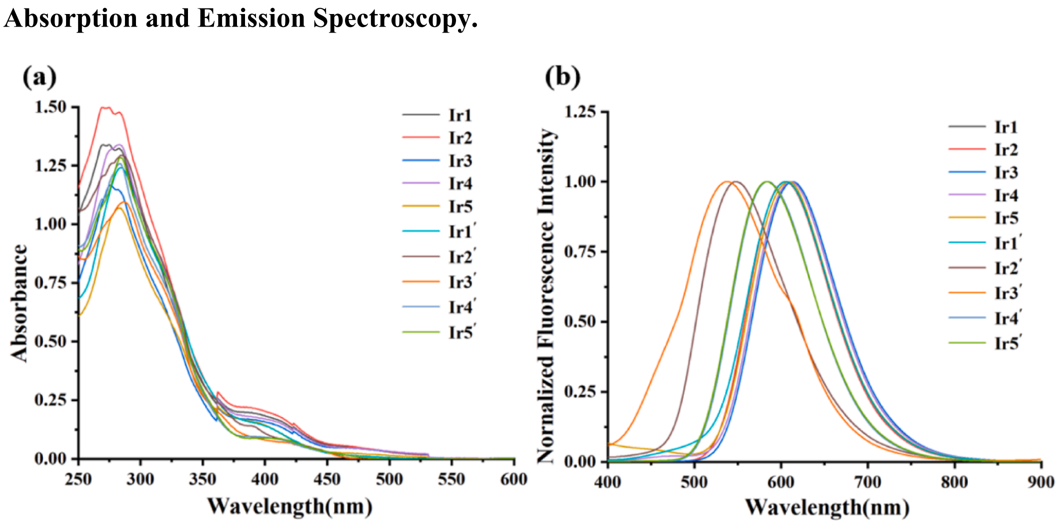

Fig. 4. (a) UV/vis absorption spectra of s **Ir1–Ir5** and **Ir1'–Ir5'** (20 μM) in methanol at 37 °C. (b) Normalized fluorescence emission spectra of **Ir1–Ir5** and **Ir1'–Ir5'** (20 μM) under the same conditions.

their suitability for further studies on anticancer activity in aqueous environments.

2.4. Cytotoxicity

The cytotoxicity of complexes **Ir1**–**Ir5** and **Ir1'**–**Ir5'** was evaluated on lung cancer A 549 cells), cervical cancer HeLa cells, and normal lung epithelial BEAS-2B cells using the MTT assay, with cisplatin serving as a reference compound (Table 1). In comparison, the cyclometalated precursors **D1-D5** and ligands **L1** and **L2** displayed minimal cytotoxicity, with IC$_{50}$ values exceeding 100 μM for both A549 and HeLa cancer cells (Table S2). Conversely, complexes **Ir1–Ir5** and **Ir1'–Ir5'** demonstrated notable cytotoxic effects on A549 and HeLa cells, with IC$_{50}$ values ranging between 3.12–53.96 μM and 3.72–82.34 μM, respectively, indicating that their cytotoxicity may arise from the coordination of metal ions with the ligands. Some of these complexes exhibited cytotoxic effects comparable to or even exceeding those of cisplatin, The incorporation of a triphenylphosphine group in complexes **Ir1–Ir5** notably enhances their cytotoxicity towards A549 and HeLa cells compared to the non-triphenylphosphine analogs **Ir1'-Ir5'** (**Ir1–Ir5**: 3.12–9.23 μM) vs. (**Ir1'-Ir5'**: 12.58–82.34 μM). This modification in **Ir1–Ir5** also improves selectivity, as evidenced by selectivity index ranging from 5.46 to 14.83 when comparing A549 cancer cells to BEAS-2B normal cells. The enhanced cytotoxicity and selectivity are likely due to the mitochondria-targeting capability conferred by the triphenylphosphine group, which allows the complexes to accumulate more effectively in cancer cell mitochondria, thereby increasing their anticancer efficacy. Given the high lipophilicity of the triphenylphosphine group, we examined whether the cytotoxicity of these complexes is influenced by their lipophilicity. To explore this, the octanol/water partition coefficients (log *P*) were determined using the shake-flask method, revealing a distinct trend in the resulting values: **Ir1** (1.35) > **Ir1'** (0.68), **Ir2** (1.07) > **Ir2'** (0.63), **Ir3** (1.22) > **Ir3'** (0.70), **Ir4** (0.98) > **Ir4'** (0.71), and **Ir5** (0.83) > **Ir5'** (0.66), indicating that triphenylphosphine-containing complexes are significantly more lipophilic. Nevertheless, comparisons among complexes with or without the triphenylphosphine group revealed that

Table 1
IC_{50} Values (μM) of Complexes **Ir1–Ir5** and **Ir1'-Ir5'** for Cancer and Normal Cell Lines, Using Cisplatin as a Control.

Complexes	IC_{50} (μM)			
	A549	HeLa	BEAS-2B	SI[a]
Ir1	3.12 ± 0.02	4.71 ± 0.26	46.28 ± 0.16	14.83
Ir2	4.21 ± 0.16	5.89 ± 0.14	46.21 ± 0.22	10.97
Ir3	5.29 ± 0.21	5.32 ± 0.17	36.18 ± 0.16	6.83
Ir4	7.26 ± 0.09	3.72 ± 0.19	43.47 ± 0.15	5.99
Ir5	9.23 ± 0.019	7.24 ± 0.19	50.45 ± 0.04	5.46
Ir1'	49.47 ± 0.27	45.81 ± 0.08	102.69 ± 0.13	2.08
Ir2'	53.96 ± 0.21	16.52 ± 0.27	91.41 ± 0.26	1.69
Ir3'	36.41 ± 0.12	82.34 ± 0.07	57.28 ± 0.19	1.57
Ir4'	25.75 ± 0.10	36.84 ± 0.12	43.71 ± 0.30	1.70
Ir5'	48.25 ± 0.15	12.58 ± 0.16	53.47 ± 0.17	1.11
Cisplatin	24.06 ± 0.08	7.41 ± 0.17	38.11 ± 0.28	1.58

[a] SI: The selectivity index is calculated as the IC_{50} ratio of BEAS-2B normal cells to A549 cancer cells. Values are presented as the mean ± standard deviation (SD) from three independent experiments. The IC_{50} values for **Ir1–Ir5** and **Ir1'–Ir5'** showed a statistically significant difference between A549 and BEAS-2B cells ($p < 0.05$).

while some correlation exists between log P values and cytotoxicity, it is not consistent across all complexes, particularly in normal cells. This suggests that lipophilicity alone may not fully explain the differences in cytotoxicity and selectivity.

2.5. *DNA binding studies*

To investigate the potential DNA binding affinity of the anticancer complexes, we first used ^1H NMR spectroscopy in an 80 % DMSO-d_6 / 20 % D_2O solution to examine interactions between the representative complexes **Ir1–Ir5** and the model nucleobase 9-methyladenine (9-MeA) (Figs. S55–59). The ^1H NMR spectra showed no significant changes over time, suggesting that these complexes did not engage in coordination reactions with 9-MeA during the 24-hour observation period. Mass spectrometry analysis also revealed no detection of nucleobase adducts (Fig. S60). Additionally, we monitored the interaction of calf thymus DNA (CT-DNA) with complexes **Ir1–Ir5** by UV–visible absorption spectroscopy (Fig. S61). CT-DNA is DNA extracted from calf thymus and is commonly used in molecular biology and drug research, especially in experiments involving the interaction of DNA with drugs or other molecules. Keeping the concentration of the complexes constant while progressively increasing the CT-DNA concentration, hyperchromicity and an approximate 5 nm blue shift were observed in the spectra of the complexes, indicating that their interaction with CT-DNA likely occurs via a noncovalent electrostatic binding mechanism [51,52]. Using the Benesi-Hildebrand equation, we determined the binding constants (K_b) for these complexes. The results revealed that the K_b values were 1.38×10^4 M^{-1} for **Ir1**, 2.83×10^4 M^{-1} for **Ir2**, 3.37×10^4 M^{-1} for **Ir3**, 5.66×10^3 M^{-1} for **Ir4**, and 7.11×10^3 M^{-1} for **Ir5**. These values are significantly lower than those reported for other DNA-binding complexes ($K_b > 10^5$ M^{-1}) [20,53,54], suggesting that these complexes exhibit relatively weak binding affinity to CT-DNA. Furthermore, the absence of coordination reactions with 9-MeA and the low nuclear co-localization efficiency observed in subsequent tests (see section “cellular localization” below) indicate that DNA binding is unlikely to play a significant role in the biological activity of these complexes.

2.6. *Albumin binding studies*

Human serum albumin (HSA) is an essential protein found in the bloodstream, responsible for transporting and metabolizing various bioactive substances. Understanding its interaction with anticancer drugs is essential for elucidating their transport, distribution, metabolism, and therapeutic effects [52]. Herein, bovine serum albumin (BSA), which shares a similar structure with HSA and is more readily available, was used as a model protein. The UV–visible absorption spectra for complexes **Ir1–Ir5** (Fig. S62) revealed a significant reduction in absorbance at 225 nm alongside a red shift, suggesting that the complexes disrupt the α-helix structure of BSA and alter the polarity of the surrounding environment upon binding [51,55,56]. In the presence of BSA, a pronounced peak at 275 nm was observed, suggesting modifications in the microenvironment of aromatic amino acids, particularly tryptophan (Trp) and tyrosine (Tyr) [56,57]. Furthermore, when the concentration of the complexes increased, the fluorescence intensity of BSA at 353 nm showed a significant reduction, indicative of a static quenching mechanism (Fig. S63) [57]. Synchronous fluorescence spectroscopy provided further insights into the structural modifications of BSA. At $\Delta\lambda = 15$ nm, the spectrum revealed features of Tyr residues, while at $\Delta\lambda = 60$ nm, it corresponded to Trp residues. Binding of complexes **Ir1–Ir5** caused a slight red shift (1–2 nm) in the emission wavelengths of both Tyr and Trp (Figs. S64 and S65), indicating alterations in their microenvironment and conformation [57,58]. These observations suggest that the complexes interact with BSA by inducing subtle structural changes in its aromatic residues.

Molecular docking studies on the **Ir1** complex were conducted using the AutoDock suite and Q-SiteFinder, tools designed to identify potential binding sites and evaluate ligand interactions with proteins. The bovine serum albumin (BSA) crystal structure (PDB ID: 4OR0) was obtained from the Protein Data Bank. Initially, Q-SiteFinder was employed to identify likely binding regions within BSA. Subsequently, docking simulations were performed using AutoDock. As AutoDock’s default force field does not include parameters for iridium, these were manually incorporated into the parameter library. Flexible residues within a 6 Å radius of the identified binding pocket were selected to allow adaptive docking. The docking results revealed several key interactions between **Ir1** and BSA, including electrostatic and hydrogen-bonding interactions (Fig. 5). Notably, salt bridges were formed with ARG217 and ARG198, while a π-cation interaction was observed with ARG217. Additionally, several “non-conventional” hydrogen bonds were identified, involving residues such as ASP450, ARG194, LEU480, GLU478, GLU353, and LEU346. These results further demonstrate the interaction between **Ir1** and BSA, providing valuable insights into the binding mechanisms and potential implications for transport, stability, and bioavailability.

2.7. *Cellular localization and cellular uptake pathway*

To investigate the potential cellular targets of these complexes, their intracellular localization within various organelles was analyzed using confocal microscopy, leveraging their fluorescent properties (Fig. 6). To visualize specific organelles, MTDR (MitoTracker Red CM-H2XRos), LTDR (LysoTracker Red DND-99), and DAPI (4,6-diamino-2-phenylindole) were used as probes for the mitochondria, lysosomes and nucleus, respectively [59,60]. A549 cells were co-stained with **Ir1–Ir5**, **Ir1'–Ir5'**, and these probes. After 1 h of treatment, clear green fluorescence was detected in the cytoplasm, confirming effective cellular uptake of both **Ir1–Ir5** and **Ir1'–Ir5'**. None of the complexes exhibited notable colocalization with DAPI or LTDR, as reflected by the low Pearson correlation coefficients (PCC: 0–0.03 for DAPI and 0.14–0.29 for LTDR), indicating minimal localization in the nucleus or lysosomes. In contrast, complexes **Ir1–Ir5** displayed strong accumulation in mitochondria, evidenced by high PCC values. (**Ir1**: 0.90; **Ir2**: 0.92; **Ir3**: 0.88; **Ir4**: 0.89; **Ir5**: 0.90). Conversely, **Ir1'–Ir5'** showed limited mitochondrial colocalization, indicated by low PCC values (**Ir1'**: 0.32; **Ir2'**: 0.38; **Ir3'**: 0.30; **Ir4'**: 0.39; **Ir5'**: 0.21). These comparisons clearly demonstrate that the introduction of the triphenylphosphine group significantly enhances the complexes’ mitochondrial targeting ability. The cytotoxic effects of these complexes are likely attributed to mitochondria-mediated cell death. Given that cancer cells possess a higher mitochondrial content than normal cells, they exhibit greater sensitivity to mitochondrial disruption. This heightened vulnerability may contribute to the enhanced anticancer selectivity (SI: 5.46–14.84) observed for the

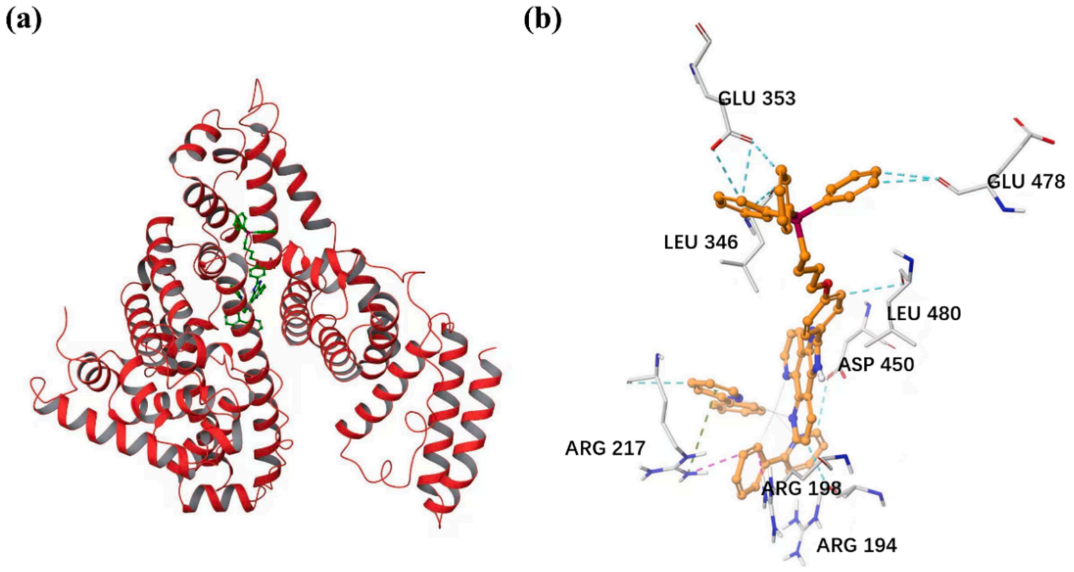

Fig. 5. (a) Docking model of complex **Ir1** positioned in the hydrophobic cavity of BSA (PDB ID: 4OR0). (b) Interaction details between complex **Ir1** and the polypeptide chains.

triphenylphosphine-based complexes in this study. Notably, the complexes **Ir1–Ir5** demonstrated significantly higher positive zeta potentials of **Ir1** (52.14 ± 0.18), **Ir2** (54.67 ± 0.23), **Ir3** (41.58 ± 0.32), **Ir4** (40.45 ± 0.26), and **Ir5** (36.55 ± 0.15) (Fig. S68), compared to the negative zeta potentials of **Ir1'** (−15.56 ± 0.21), **Ir2'** (−13.79 ± 0.23) **Ir3'** (−11.06 ± 0.32), **Ir4'** (−16.27 ± 0.26), and **Ir5'** (−19.63 ± 0.15) respectively (Fig. S69). This property could improve mitochondrial targeting, as mitochondria have negatively charged surfaces within the cytosol. The elevated positive zeta potentials of **Ir1–Ir5** may facilitate their preferential accumulation in cancer cell mitochondria, which typically have higher membrane potentials than those in normal cells [61], potentially enhancing their effectiveness as targeted anticancer agents. Furthermore, the markedly higher log *P* values of **Ir1–Ir5** compared to **Ir1'-Ir5'**, as discussed in section on cytotoxicity, may further support their mitochondrial localization. Generally, highly lipophilic anticancer complexes can disrupt cellular metabolic balance and increase intracellular ROS levels by intensifying interactions with mitochondrial membranes [62]. Cellular uptake of small molecule complexes can occur through energy-dependent or energy-independent mechanisms [59]. Laser confocal microscopy was used to examine the cellular uptake of complexes **Ir1** and **Ir1'** in A549 cells. Following 1 h of incubation, clear green fluorescence was observed in the cytoplasm, confirming successful penetration (Fig. 7). However, at 4 °C or with the metabolic inhibitor CCCP, fluorescence intensity dropped significantly, indicating that the uptake of both triphenylphosphine-containing and non-triphenylphosphine complexes relies on energy. In contrast, treatment with the endocytosis inhibitor chloroquine did not alter intracellular fluorescence levels compared to the 37 °C control, ruling out endocytosis as the primary uptake mechanism for **Ir1** and **Ir1'**.

2.8. *Mitochondrial membrane depolarization*

Due to the preferential accumulation of these cyclometalated complexes in mitochondria, their effects on mitochondrial function were further investigated. The mitochondrial membrane potential (MMP, $\triangle\psi m$), an essential electrical gradient for cellular activity, is crucial for mitochondrial integrity. The loss of MMP is a critical early step in initiating apoptosis, triggering a series of biochemical changes within the mitochondrial membrane that ultimately result in cell death [47,63–66]. To assess changes in MMP, flow cytometry with the JC-1 fluorescent probe was used on A549 and BEAS-2B cells incubated with complexes **Ir1** and **Ir1'**. JC-1, known for its color-shifting properties, is ideal for detecting MMP variations. Under high MMP conditions, JC-1 aggregates in the mitochondrial matrix as J-aggregates, emitting red fluorescence. In contrast, at low MMP levels, JC-1 remains as monomers, producing green fluorescence. The red-to-green fluorescence shift provides a straightforward way to monitor reductions in MMP. A549 cells were treated with **Ir1** and **Ir1'** at concentrations of 0.5 and 1.0, and **Ir1** significantly reduced MMP in these cells compared to the untreated controls. As **Ir1** concentration of increased from 0 to 2 × IC_{50}, the proportion of cells showing mitochondrial membrane depolarization significantly rose by 60.1 %, from 20.1 % to 85.1 % (Fig. 8a, d), closely matching the depolarization level of the positive control (67.2 %). In contrast, **Ir1** treatment in BEAS-2B normal cells and **Ir1'** treatment in A549 cells resulted in minimal depolarization, measuring 15.6 % and 25.2 %, respectively (Fig. 8b, e and 8c, f). These findings align with the observed cytotoxicity and anticancer selectivity, with **Ir1** exhibiting greater specificity for A549 cancer cells compared to BEAS-2B normal cells. Furthermore, **Ir1** demonstrated stronger cytotoxic effects against both A549 and HeLa cancer cells than **Ir1'**. This suggests that the inclusion of the triphenylphosphine moiety enhances the anticancer potency of the complexes by specifically targeting mitochondria and disrupting their function.

2.9. *Cellular ROS determination*

Many studies have demonstrated that impaired mitochondria lose their ability to regulate ROS production efficiently, leading to heightened oxidative stress within cancer cells [67,68] Given that cancer cells generally experience higher oxidative stress than normal cells, further ROS elevation induced by anticancer complexes is less likely to disrupt the oxidative equilibrium in normal cells, potentially contributing to the selectivity of these agents [68–70]. The impact of varying concentrations (0.5, 1.0, and 2.0 × IC_{50}) of **Ir1** and **Ir1'** complexes on ROS levels in A549 cancer cells and BEAS-2B normal cells was evaluated using the fluorescent probe DCFH-DA and observed under a fluorescence microscope (Fig. 9). It is important to note that this assay measures overall oxidative stress rather than quantifying specific ROS. A549 cells treated with complex **Ir1** showed a marked, concentration-dependent increase in fluorescence intensity, correlating directly with elevated ROS levels compared to untreated controls (Fig. 9a, d). This trend highlights the ability of these complexes to disrupt cellular redox balance by

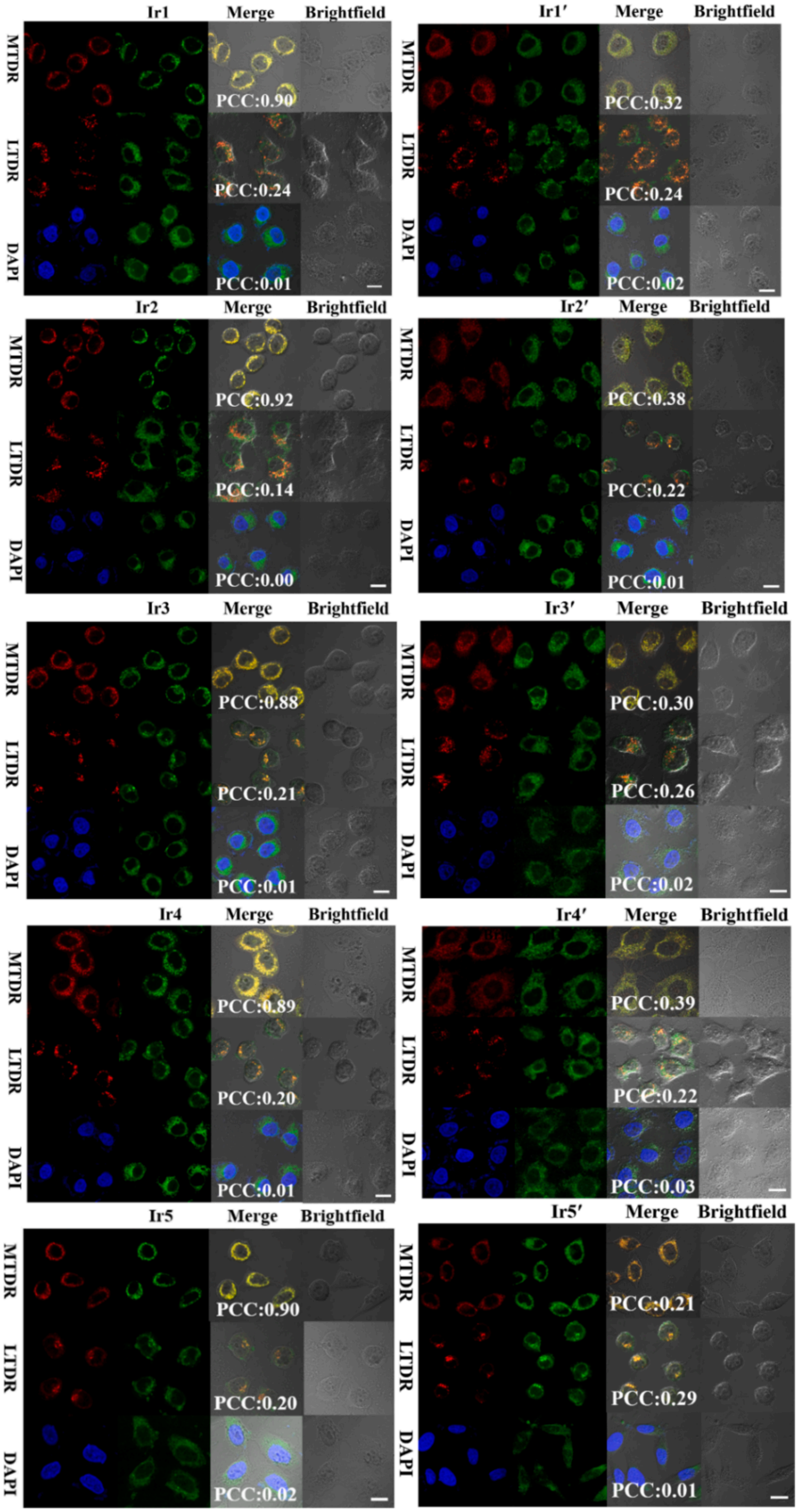

Fig. 6. Confocal microscopy analysis of the intracellular localization of **Ir1–Ir5** and **Ir1'–Ir5'**. A549 cells were treated with **Ir1–Ir5** and **Ir1'–Ir5'** (2 μM) for 1 h at 37 °C, followed by co-staining with DAPI (1 μg/mL), MTDR (500 nM), or LTDR (75 nM) for another hour. Scale bar: 20 μm. Green fluorescence indicates **Ir1–Ir5** and **Ir1'–Ir5'**, red represents mitochondria or lysosomes, and blue corresponds to the nucleus. (For interpretation of the references to color in this figure legend, the reader is referred to the web version of this article.)

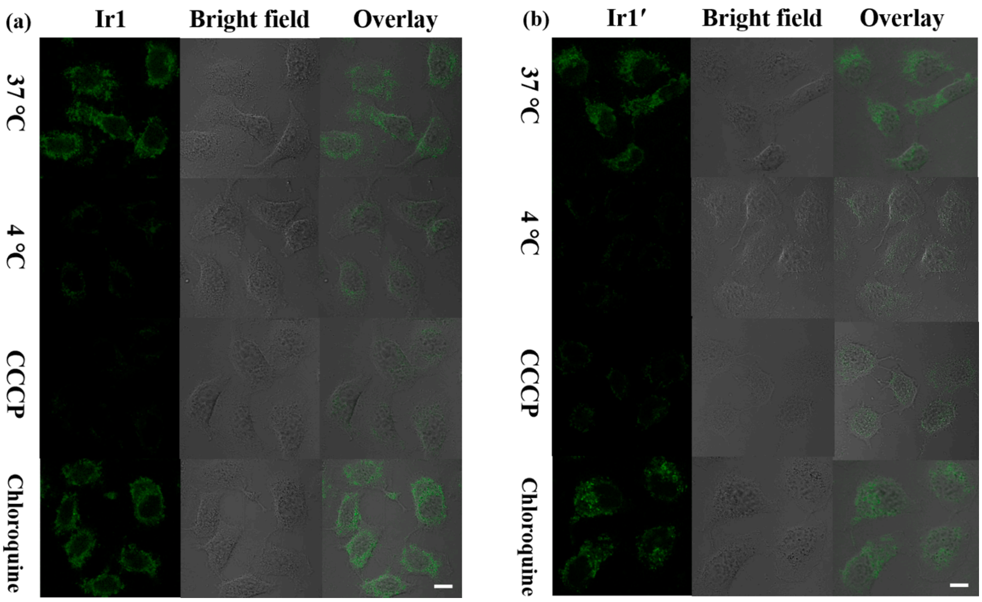

Fig. 7. Influence of temperature (37 °C or 4 °C), chloroquine (50 μM), and CCCP (50 μM) on the uptake of **Ir1** (2 μM) (a) and **Ir1'** (2 μM) (b) by cells. Scale bar: 20 μm, $\lambda_{ex} = 405$ nm, $\lambda_{em} = 430–490$ nm.

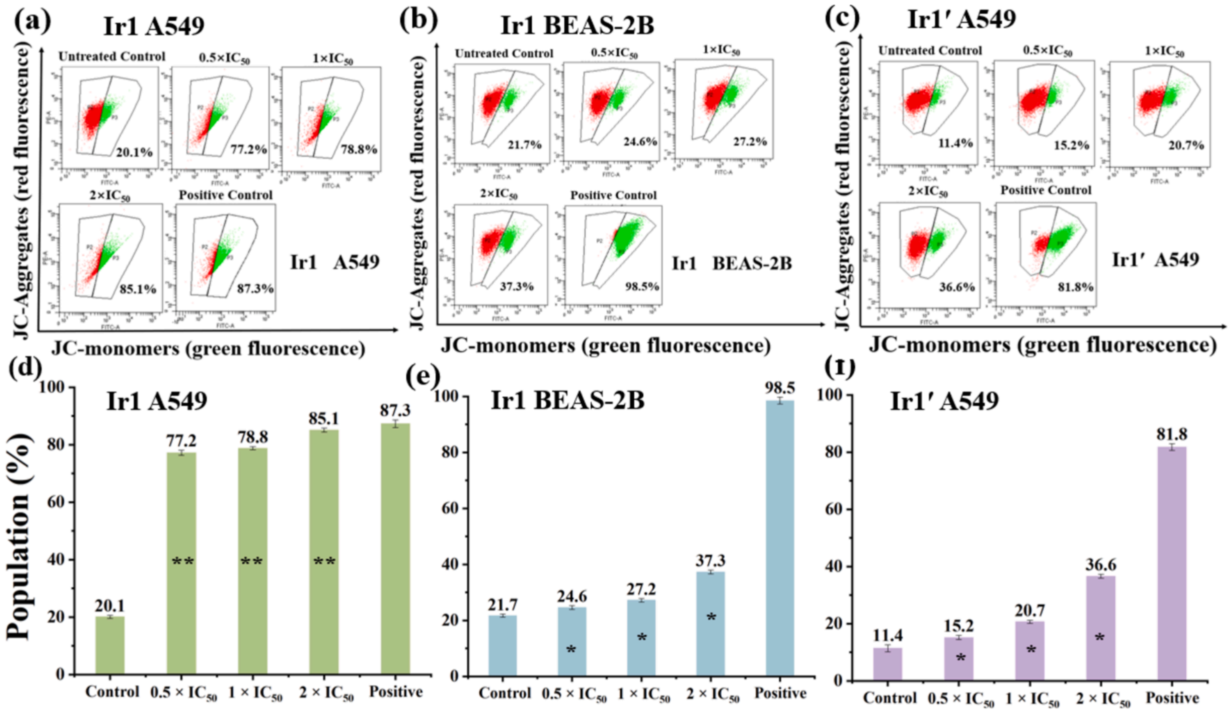

Fig. 8. (a, d) Effects of **Ir1** on the MMP in A549 cancer cells. (b, e) Effects of **Ir1** on the MMP in BEAS-2B cells. (c, f) Effects of **Ir1'** on the MMP in A549 cancer cells. CCCP (Carbonyl cyanide *m*-chlorophenyl hydrazone) served as a positive control for inducing mitochondrial membrane depolarization. Data are presented as mean ± SD from three replicates. Statistical significance compared to the untreated control: $^*p < 0.05$, $^{**}p < 0.01$.

promoting ROS generation [51,71,72]. However, the changes of ROS levels in BEAS-2B cells following an increase in **Ir1** concentration were negligible (Fig. 9b, e). At the same concentration, the fluorescence intensity of **Ir1'** in A549 cells, representing ROS levels, was notably lower compared to **Ir1** (Fig. 9a vs. Fig. 9c). This observation aligns with the anticancer activity and selectivity of the iridium^{III} complexes, as **Ir1** exhibited selective cytotoxicity toward A549 cancer cells over BEAS-2B normal cells. Collectively, these findings suggest that increased ROS production is a key mechanism driving the action of these complexes.

2.10. *Apoptosis*

Anticancer complexes with high ROS generation can disrupt the cellular redox balance, inducing apoptosis and cellular damage [73]. The mechanism of apoptosis-induced cell death was evaluated with the annexin V/PI assay. A549 cancer cells were treated with **Ir1** and **Ir1'** at 0.25, 0.5, and 1 × IC_{50} for 48 h and analyzed by flow cytometry (Fig. 10). Both complexes exhibited a concentration-dependent rise in the late apoptotic cell population. Specifically, 88.28 % of A549 cells treated with **Ir1** at 1 × IC_{50} underwent late apoptosis (Fig. 10a). The

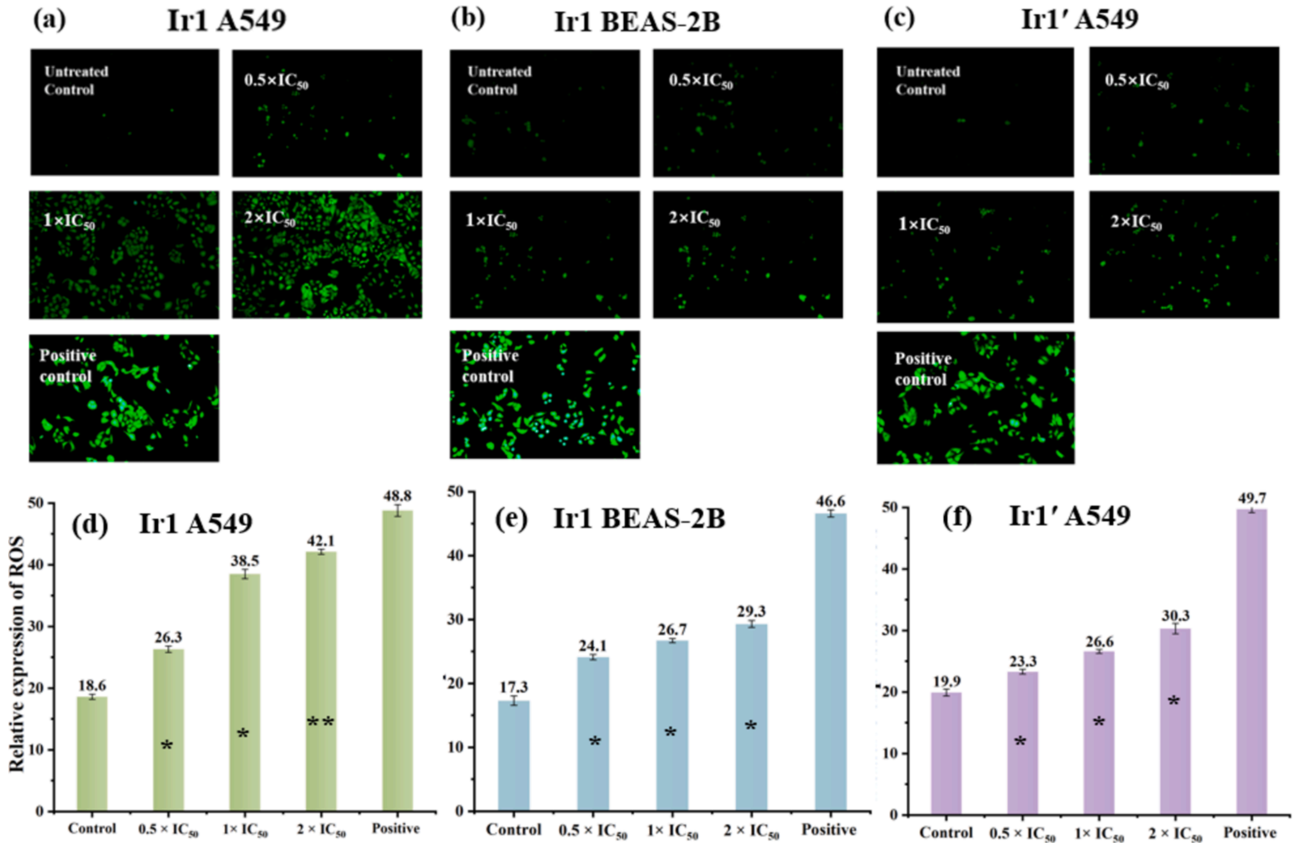

Fig. 9. Fluorescence microscopy analysis of ROS levels in A549 cells treated with **Ir1** (a, d) and **Ir1'** (c, f) and in BEAS-2B cells treated with **Ir1** (b, e) for 24 h at 37 °C. Cells were stained with DCFH-DA, and ROSup served as a positive control for ROS induction. Data are presented as mean ± SD from three replicates. Statistical significance compared to untreated controls: $^{*}p < 0.05$, $^{**}p < 0.01$.

impact of **Ir1** on BEAS-2B normal cells was evaluated under the same conditions (Fig. 10b). At 1 × IC_{50}, only 11.75 % of cells were in the late apoptotic stage, showing minimal change compared to the untreated control. In contrast, **Ir1'** exhibited a more pronounced concentration-dependent effect on A549 cells, with late apoptotic populations increasing from 12.1 % to 14.28 % and then to 16.08 % as the concentration rose (Fig. 10c). These results are consistent with the low cytotoxicity of **Ir1** in normal cells and confirm that these complexes induce apoptosis as the primary mode of cell death.

Among the various genes that regulate apoptosis, the Bcl-2 protein family, including B cell CLL/Bcl-2, has received significant scientific interest. Bax, a key pro-apoptotic protein, is instrumental in maintaining the balance between cell survival and programmed death. Upon stimulation, Bax downregulates Bcl-2 expression, shifting the balance toward apoptosis [74,75]. In this study, Western blotting was employed to quantify Bax and Bcl-2 protein levels to confirm the involvement of the mitochondrial apoptosis pathway. Fig. 11 demonstrates that as **Ir1** concentration increases, Bcl-2 levels significantly decrease, while Bax levels rise correspondingly. These changes indicate that **Ir1** promotes apoptosis in A549 cells through the mitochondrial pathway. This conclusion aligns with the findings of the co-localization analysis.

2.11. *Cell cycle arrest*

Cell cycle arrest, often triggered by apoptotic signals, plays a critical role in facilitating apoptosis. Many anticancer complexes exert their effects by disrupting the cell cycle [76]. To evaluate this, we used flow cytometry to analyze the impact of **Ir1** (containing a triphenylphosphine moiety) and **Ir1'** (without the triphenylphosphine moiety) on cell cycle progression in A549 cancer cells. After 24 h of treatment at 0.25 × IC_{50} and 0.5 × IC_{50}, a concentration-dependent rise in the G_2/M phase population was observed, alongside a decrease in the s and G_0/G_1 phases (Figs. 12a, b, S66, and S67). At 0.5 × IC_{50}, the G_2/M phase population increased by 10.16 % for **Ir1** and 3.67 % for **Ir1'** compared to untreated controls. These results demonstrate that both complexes, with or without the triphenylphosphine moiety, induce G_2/M phase arrest.

2.12. *Inhibition of cell migration*

Reduced surface adhesion can facilitate the migration of cancer cells from the original tumor to other organs, making the prevention of metastasis a critical challenge in cancer therapy [77,78]. Cell migration, metastasis and invasion are heavily influenced by extracellular matrix degradation and changes in cell adhesion molecules. To investigate the effect of the representative complex **Ir1** on the migration of A549 cancer cells, a wound-healing assay was conducted, as shown in Fig. 13. Treatment with 0.5 × IC_{50} of **Ir1** reduced the wound closure rate (WCR) in A549 cells to 12.87 %, compared to 41.51 % in the control group. **Ir1** also demonstrated a dose-dependent reduction in WCR in A549 cancer cells. These observations suggest that these cyclometalated iridium^{III} complexes effectively inhibit A549 cell migration in vitro.

3. Conclusions

In this work, we developed and prepared a set of triphenylphosphine-modified cyclometalated iridium^{III} complexes designed to selectively target mitochondria in cancer cells. The inclusion of the triphenylphosphine group significantly enhanced mitochondrial localization and cytotoxicity in cancer cells while maintaining selectivity over normal cells. Through comprehensive cellular analyses, these complexes demonstrated the ability to effectively depolarize mitochondrial membrane potential, increase ROS production and trigger intrinsic apoptosis.

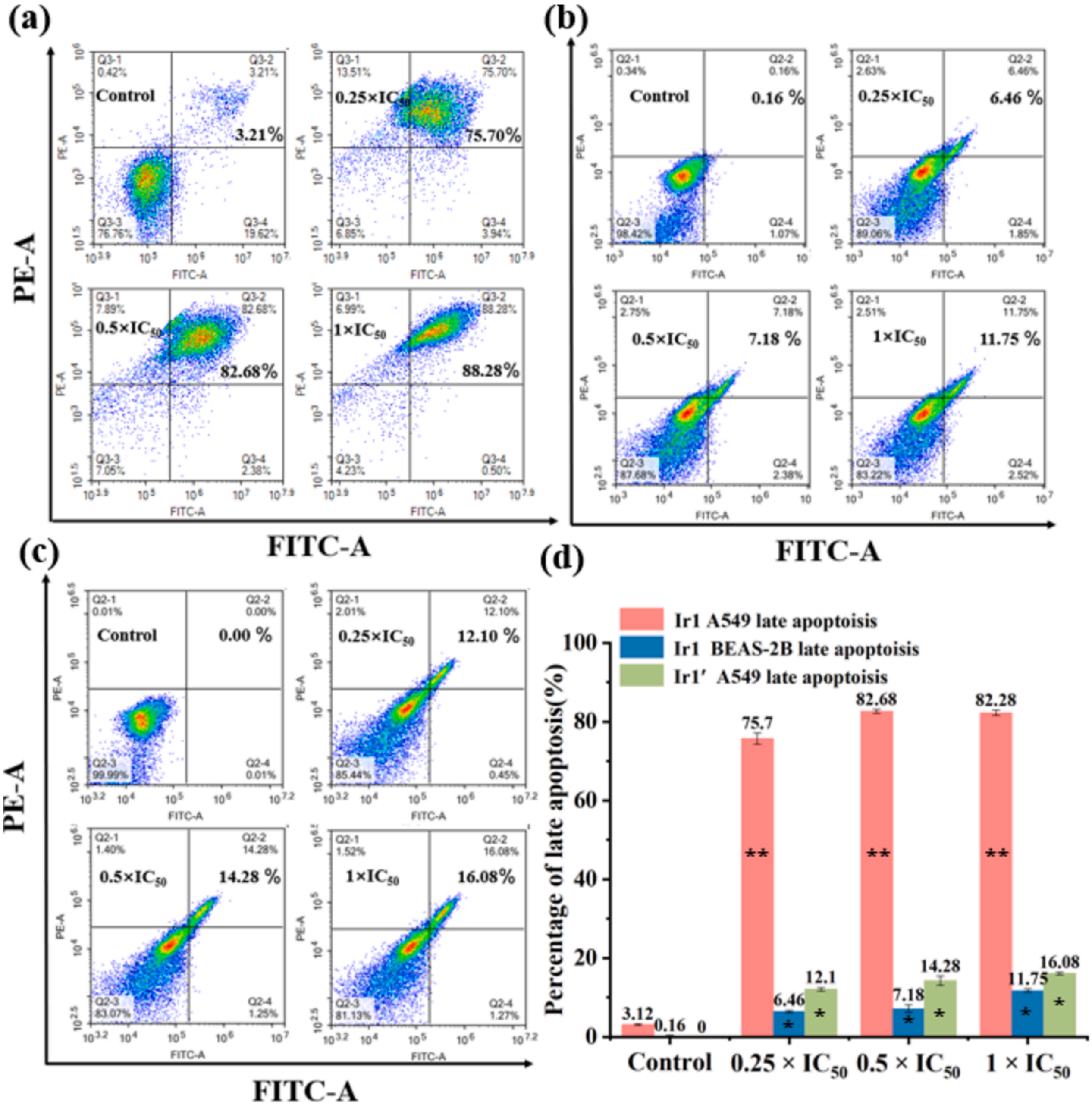

Fig. 10. Cell apoptosis analysis by flow cytometry. (a) A549 cells untreated (control) or treated with various concentrations of **Ir1** for 48 h. (b) BEAS-2B cells untreated (control) or treated with Ir1 for 48 h. (c) A549 cells untreated (control) or treated with **Ir1'** at different concentrations for 48 h. (d) Apoptosis histograms for A549 and BEAS-2B cells treated with **Ir1** and **Ir1'** at 0.25 × IC_{50}, 0.5 × IC_{50}, and 1 × IC_{50} for 48 h. Data are presented as mean ± SD from three replicates. Statistical significance compared to the control: *$p < 0.05$, **$p < 0.01$.

Moreover, the promotion of G_2/M phase cell cycle arrest and inhibition of cell migration were also observed for these complexes, indicating multiple pathways for their anticancer action. These observations highlight the role of the triphenylphosphine moiety in augmenting both the anticancer efficacy and selective mitochondrial targeting of these complexes. Moreover, these triphenylphosphine-modified iridium^{III} complexes integrate imaging capabilities with anticancer effects, presenting a promising approach for developing multifunctional theranostic agents.

4. Experimental section

The Supplementary materials include comprehensive details, covering general procedures and the preparation of ligands **L1** and **L2**, which were synthesized following adapted protocols from the literature [79,80]. The synthesis of metal precursors **D1–D5** was carried out using previously reported methodologies [18,44]. Further descriptions of the biological assays and experimental protocols are also provided in the supplementary materials for reference.

4.1. Synthesis of complexes

General Procedure: The reaction involved mixing cyclometalated iridium(III) precursors (1 eq.), ligands (2 eq.), and an excess of NH_4PF_6 (2 eq.) in a CH_2Cl_2/CH_3OH solution at a 1:1 ratio (v/v). The mixture was stirred at room temperature for 24 h to ensure reaction completion. Afterward, the solvents were evaporated under reduced pressure to yield a crude solid. This solid was dissolved in CH_2Cl_2, filtered to eliminate

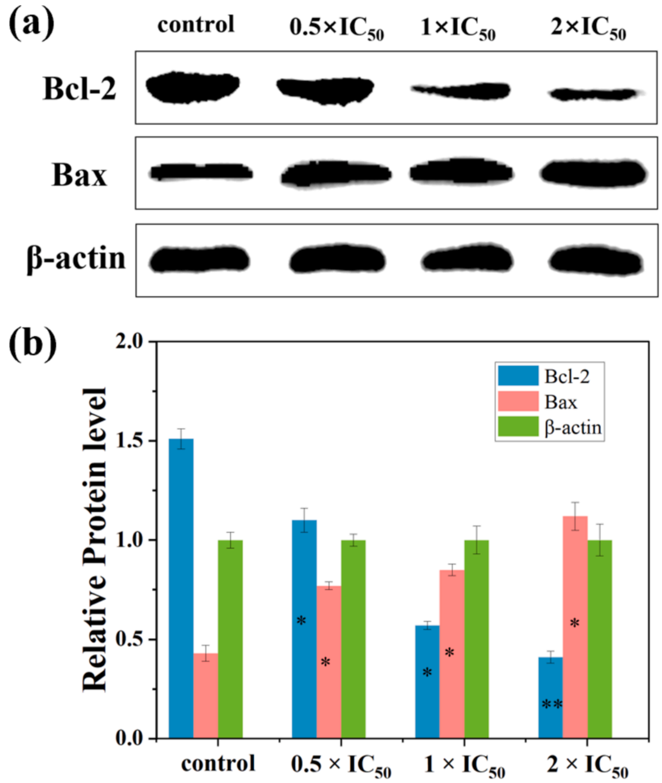

Fig. 11. (a) Protein expression levels analyzed by Western blot after 24 h treatment with **Ir1** at concentrations of 0.5, 1.0, and 2.0 × IC_{50}. (b) Histograms showing protein expression levels at various **Ir1** concentrations. Data represent the mean ± SD from three independent experiments. Statistical significance compared to the control: $^*p < 0.05$, $^{**}p < 0.01$.

impurities, and then was concentrated. Finally, the product was purified through recrystallization using CH_2Cl_2 and *n*-hexane, yielding a light yellow solid.

Ir1: isolated yield 69 mg (49 %). ^{1}H NMR (500 MHz, DMSO-d_6) δ 9.19 (d, 2H), 8.27 (m, 4H), 8.16 (s, 2H), 8.09 (s, 2H), 7.97 (d, 2H), 7.94 (m, 5H), 7.81 (m 12H), 7.51 (s, 2H), 7.17 (d, 2H), 7.08 (t, 2H), 7.02 (m, 4H), 6.31 (d, 2H), 4.17 (t, 2H, OCH_2), 3.75 (m, 2H, OCH_2CH_2), 2.03 (m, 2H P-CH_2CH_2), 1.81 (m, 2H, P-CH_2CH_2). ^{13}C NMR (126 MHz, DMSO-d_6) δ 167.38, 160.77 (*C*—O), 153.28, 150.86 (*C*═N), 149.60, 148.80, 144.47, 139.16, 135.61 (P-Ph_3), 134.04, 132.64, 131.72, 130.76 (P-Ph_3), 128.73 (*C*—N), 127.48 (*C*-NH), 125.53, 124.30, 122.84, 120.44, 119.30, 118.61, 115.64, 66.82 (OCH_2), 20.46 (O-CH_2CH_2), 20.06(P-CH_2), 18.95 (P-CH_2CH_2). ESI-MS (*m/z*): calcd for $C_{63}H_{49}IrN_6OP$ 1129.3329, found: 1129.3446 $[M-H-2PF_6]^+$. ^{31}P NMR (202 MHz, DMSO-d_6): δ −151.22, −147.71, −144.20, −140.68, −137.17, 24.06. Elemental analysis: calcd for $C_{63}H_{50}IrN_6OP_3F_{12}$: C, 53.28; H, 3.55; N, 5.92. found: C, 53.53; H, 3.37; N, 6.71.

Ir2: isolated yield 61 mg (43 %).^{1}H NMR (500 MHz, DMSO-d_6) δ 9.22 (d, 2H), 8.30 (d, 2H), 8.23 (d, 2H), 8.18 (d, 1H), 8.11 (m, 2H), 7.98 (m, 4H), 7.90 (m, 7H), 7.83 (m, 10*H*), 7.48 (d, 2H), 7.19 (d, 2H), 6.98 (m,3H), 6.12 (s, 2H), 4.19 (t, OCH_2,2H), 3.76 (m, OCH_2CH_2,2H), 2.13 (s, 6H, Ph-CH_3), 2.04 (m, 2H, P-CH_2CH_2), 1.79 (m, 2H,P-CH_2CH_2). ^{13}C NMR (126 MHz, DMSO-d_6) δ 167.41, 160.75 (*C*—O), 153.28, 151.22 (*C*═N), 149.41, 148.76, 144.40, 141.89, 140.10, 139.00, 135.49 (P-Ph_3), 134.04, 132.50, 132.21, 130.76 (P-Ph_3), 128.73 (*C*—N), 127.45 (*C*-NH), 125.48, 123.80, 122.35, 120.04, 119.30, 118.62, 115.62, 66.81 (OCH_2), 31.41(O-CH_2CH_2), 22.52 (P-CH_2), 22.03 (Ph-CH_3), 14.42 (P-CH_2CH_2). ^{31}P NMR (202 MHz, DMSO-d_6): δ 24.07, −151.21, −147.70, −144.19, −140.67, −137.16. ESI-MS (*m/z*): calcd for $C_{65}H_{53}IrN_6OP$ 1157.3642, found:1157.3772, $[M-H-2PF_6]^+$. Elemental analysis: calcd for: $C_{65}H_{54}IrN_6O\ P_3F_{12}$: C, 53.91; H, 3.76; N, 5.80. found: C, 54.02; H, 3.56; N, 6.62.

Ir3: isolated yield 71 mg (48 %).^{1}H NMR (500 MHz, DMSO-d_6) δ 9.20 (d, 2H), 8.28 (d, 2H), 8.23 (d, 1H), 8.15 (m, 3H), 7.92 (t, 5H), 7.87 (m, 16H), 7.41 (d, 2H), 7.17 (d, 2H), 6.89 (t, 2H), 6.70 (d, 2H), 5.74 (d, 2H), 4.18 (t, 2H, OCH_2CH2), 3.71 (m, 2H, OCH_2CH_2), 3.59 (s, 6H, OCH_3), 2.00 (m, 6.5 Hz, 2H, P-CH_2CH_2), 1.78 (m, 2H, P-CH_2CH_2). ^{13}C NMR (126 MHz, DMSO-d_6) δ 167.20, 160.99 (*C*—O), 153.29, 153.06 (*C*═N), 149.24, 148.81, 144.38, 138.85, 137.30, 135.41 (P-Ph_3), 134.01, 130.74 (P-Ph_3), 128.79, 127.62 (*C*—N), 127.30 (*C*-NH), 122.90, 122.38, 119.58, 119.27, 118.59, 117.19, 115.56, 107.73, 66.75 (OCH_2), 54.91 (OCH_3), 29.53 (O-CH_2CH_2), 18.92 (P-CH_2), 14.40 (P-CH_2CH_2). ^{31}P NMR (202 MHz, DMSO-d_6): δ −151.21, −147.70, −144.19, −140.67, −137.16, 24.07. ESI-MS (*m/z*): calcd for, $C_{65}H_{53}IrN_6O_3P$ 1189.3541, found 1189.3678, $[M-H-2PF_6]^+$. Elemental analysis: calcd for: $C_{65}H_{54}IrN_6O_3P_3F_{12}$:C, 52.74; H, 3.68; N, 5.68. found: C, 52.92; H, 3.51; N, 5.50.

Ir4: isolated yield 78 mg (53 %).^{1}H NMR (500 MHz, DMSO-d_6) δ 9.24 (d, 2H), 8.33 (m, 3H), 8.24 (d, 2H), 8.11 (m, 2H), 7.99 (t, 2H), 7.92 (t, 3H), 7.87 (m, 15H), 7.57 (d, 2H), 7.18 (d, 2H), 7.10 (m, 4H), 5.73 (d, 2H), 4.18 (t, 2H, OCH_2CH_2), 3.75 (m, 2H, OCH_2CH_2), 2.03 (m, 2H, P-CH_2CH_2), 1.77 (m, 2H, P-CH_2CH_2). ^{13}C NMR (126 MHz, DMSO-d_6) δ 163.29, 162.32, 160.81 (*C*—O), 155.02, 153.39 (*C*═N), 150.34, 149.33, 144.09, 140.39, 135.48 (P-Ph_3), 134.05, 133.30, 130.76 (P-Ph_3), 128.84, 128.29 (*C*—N), 127.78 (*C*-NH), 124.90, 123.79, 122.24, 119.31,

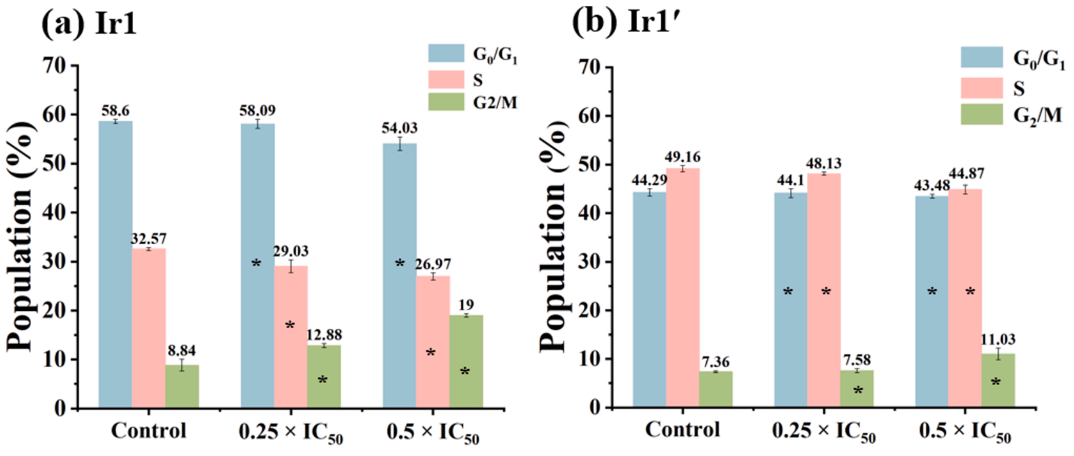

Fig. 12. Flow cytometry results showing the cell cycle distribution of A549 cancer cells treated with **Ir1** (a) and **Ir1'** (b) at concentrations of 0.25 × IC_{50} and 0.5 × IC_{50}. Cells were stained using PI/RNase prior to analysis. Data represent the mean ± standard deviation (SD) from three independent experiments. Statistical significance was determined in comparison to untreated controls, with $^*p < 0.05$ and $^{**}p < 0.01$.

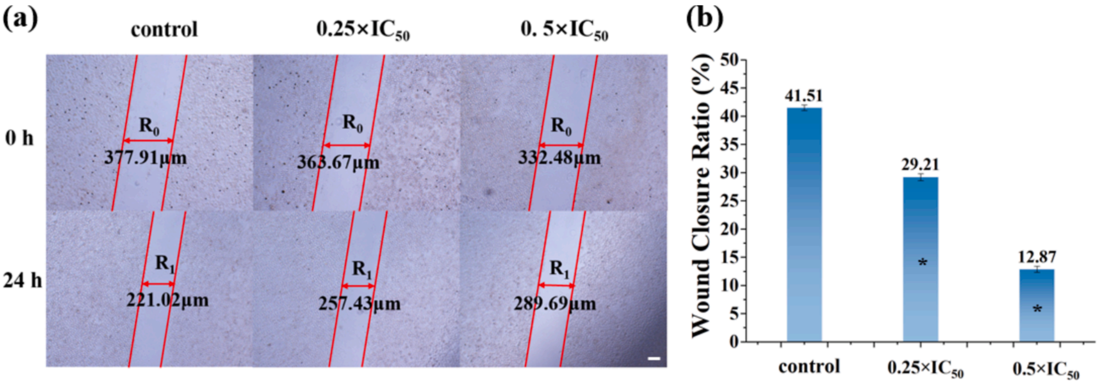

Fig. 13. (a) Wound-healing assay of A549 cells after 24 h treatment with **Ir1**. (b) Histogram analysis of wound closure rates after 24 h treatment. Representative images were taken at 0 h and 24 h, with wound widths marked (μm). Scale bar: 100 μm. Wound closure rate was calculated as $(R_0 - R_1)/R_0 \times 100$ %. Data are presented as mean ± SD from three replicates. Statistical significance compared to the control: $^*p < 0.05$, $^{**}p < 0.01$.

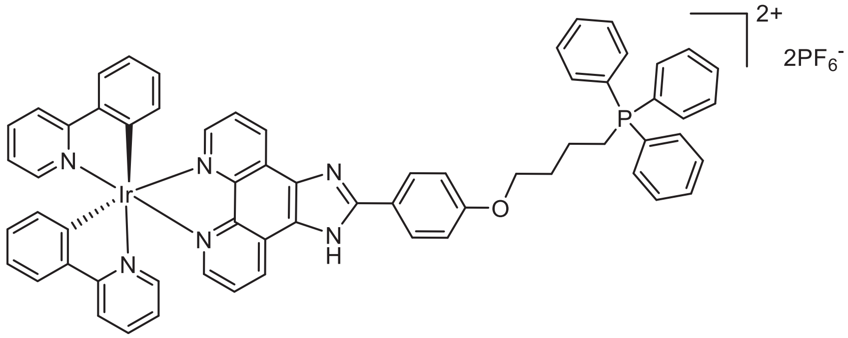

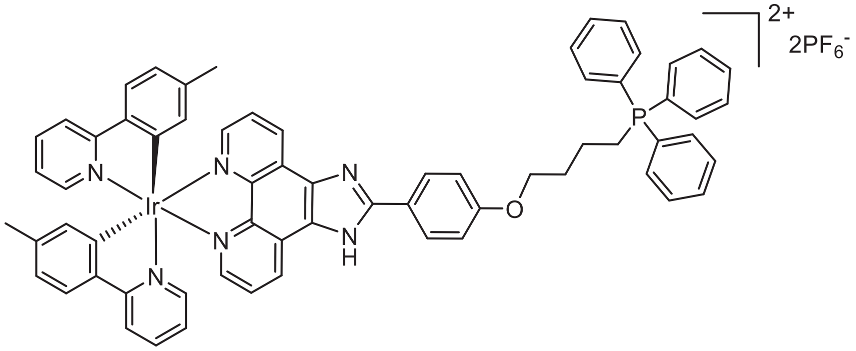

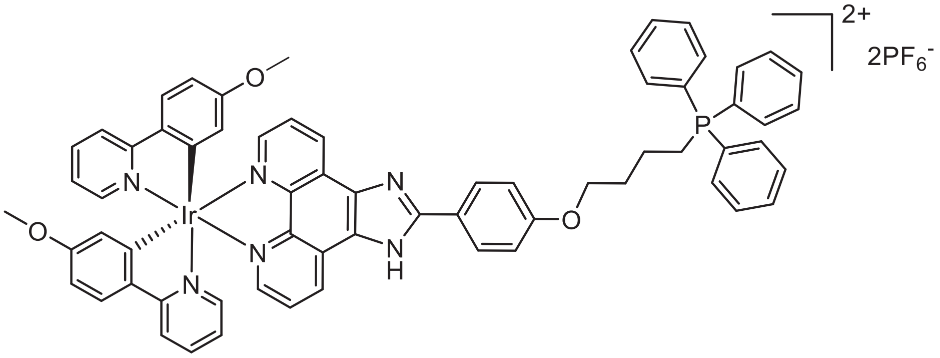

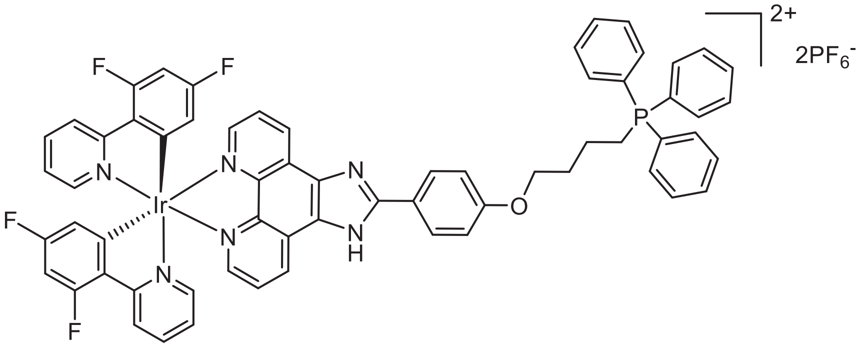

118.62, 115.63, 113.87, 99.58, 66.80 (O*C*H_2), 31.41 (O-CH_2*C*H_2), 22.52 (P-*C*H_2), 14.40 (P-CH_2*C*H_2). ^{31}P NMR (202 MHz, DMSO-*d*$_6$): δ −151.22, −147.71, −144.19, −140.68, −137.17, 24.06. ^{19}F NMR (471 MHz, DMSO-*d*$_6$): δ −69.41 (s), −70.92 (s), −106.61 (d), −108.81 (d). ESI-MS (*m/z*): calcd for $C_{63}H_{49}IrN_6OPF_2$ 1201.3031, found: 601.1616 $[(M{-}2PF_6)/2]^+$. Elemental analysis: calcd for $C_{63}H_{50}IrN_6OP_3F_{14}$: C, 51.96; H, 3.32; N, 5.77. found: C, 52.13; H, 3.07; N, 5.53.

Ir5: isolated yield 64 mg (47 %).^{1}H NMR (500 MHz, DMSO-*d*$_6$) *δ* 9.18 (d, 2H), 8.87 (d, 2H), 8.28 (m, 3H), 8.13 (m, 2H), 7.92 (m, 4H), 7.87 (m, 15H), 7.17 (d, 2H), 7.09 (m, 3H), 6.91 (m, 2H), 6.60 (m, 2H), 6.30 (m, 2H), 4.17 (m, 2H, O*CH*$_2$$CH_2$), 3.78 (m, 2H, OCH_2*CH*$_2$), 2.04 (m, 2H, P-CH_2*CH*$_2$), 1.77 (m,2H, P-*CH*$_2$$CH_2$). ^{13}C NMR (126 MHz, DMSO-*d*$_6$) *δ* 160.79 (*C*—O), 153.11 (*C*═N), 149.17, 145.19, 143.63, 139.44, 135.64 (P-Ph_3), 134.05, 133.18, 132.73, 130.78 (P-Ph_3), 129.08, 128.75, 127.34 (*C*—N), 126.99 (*C*-NH), 123.55, 122.19, 119.30, 118.62, 115.62, 112.58, 108.89, 66.81 (O*C*H_2), 31.41 (O-CH_2*C*H_2), 22.52 (P-*C*H_2), 14.42 (P-CH_2*C*H_2). ^{31}P NMR (202 MHz, DMSO-*d*$_6$): δ −154.75. −147.70, −144.19, −140.68, −137.68, −133.65, 24.07. ESI-MS (*m/z*): calcd for $C_{59}H_{46}IrN_8OP$ 1107.3234, found: 1107.3236 and 554.1661 $[M{-}H{-}2PF_6]^+$. Elemental analysis: calcd for $C_{59}H_{47}IrN_8OP_3F_{12}$: C, 50.72; H, 3.39; N, 8.02. found: C, 50.94; H, 3.55; N,8.21.

Ir1': isolated yield 65 mg (61 %).^{1}H NMR (500 MHz, DMSO-*d*$_6$) *δ* 14.53 (s ,1H, N*H*), 9.38 (s, 1H), 9.18 (s, 1H), 8.32 (d, 2H), 8.27 (d, 2H), 8.15 (d, 2H), 8.07 (s, 2H), 7.96 (d, 2H), 7.88 (t, 2H), 7.51 (d, 2H), 7.19 (d, 2H), 7.07 (t, 2H), 7.02 (m, 4H), 6.30 (d, 2H), 4.10 (t, 2H, O*CH*$_2$), 1.80 (m, 2H, OCH_2*CH*$_2$), 1.47 (m, 2H, *CH*$_2$$CH_3$), 0.97 (t, *CH*$_3$). ^{13}C NMR (126 MHz, DMSO-*d*$_6$) *δ* 167.37, 160.75 (*C*—O), 153.36, 151.02, 149.68, 144.51, 139.13, 131.70, 130.70, 128.90 (*C*—N), 125.52, 124.31, 122.78 (*C*-NH), 122.27, 120.41, 115.22, 67.86 (O*C*H_2), 31.15 (OCH_2*C*H_2), 19.21 (*C*H_2CH_3), 14.19 (CH_2*C*H_3). ESI-MS (*m/z*): calcd for $C_{45}H_{36}IrN_6O$ 869.2580, found: 869.2700 $[M{-}PF_6]^+$. ^{31}P NMR (202 MHz, DMSO-*d*$_6$): δ-151.21, −147.70, −144.18, −140.67, −137.16. Elemental analysis: calcd for $C_{45}H_{36}IrN_6OPF_6$: C, 53.30; H, 3.58; N, 8.29. found: C, 53.53; H, 3.37; N, 8.01.

Ir2': isolated yield 65 mg (55 %).^{1}H NMR ($CDCl_3$, 500 MHz) *δ* 15.43 (s ,1H, N*H*), 10.51 (s, 1H), 9.22 (s, 1H), 8.69 (d, 2H), 8.11 (s, 2H), 7.87 (d, 2H), 7.75 (s, 2H), 7.70 (m, 4H), 7.31 (d, 2H), 7.04 (d, 2H), 6.91 (d, 2H), 6.78 (s, 2H), 6.21 (s, 2H), 4.03 (t, 2H, O*CH*$_2$), 2.18 (s, 6H, Ph-*CH*$_3$), 1.83 (m, 2H, OCH_2*CH*$_2$), 1.51 (m, 2H, *CH*$_2$$CH_3$), 0.99 (t, 3H, $_2$*CH*$_3$) ^{13}C NMR (126 MHz, DMSO-*d*$_6$) *δ* 167.42, 160.94, 153.23, 151.23, 149.42, 148.69, 144.34, 141.88, 140.09, 139.01, 132.47, 128.64 (*C*—N), 127.35, 125.47, 123.80, 122.04 (*C*-NH), 120.04, 115.45, 67.93 (O*C*H_2), 31.15 (OCH_2*C*H_2), 22.03 (C-*C*H_3), 19.20 (*C*H_2CH_3), 14.18 (CH_2*C*H_3). ^{31}P NMR (202 MHz, DMSO-*d*$_6$): δ −151.22, −147.71, −144.19, −140.68, −137.17. ESI-MS (*m/z*): calcd for $C_{47}H_{40}IrN_6O$ 897.2891, found: 897.3020 $[M{-}PF_6]^+$. Elemental analysis: calcd for $C_{47}H_{40}IrN_6OPF_6$: C, 54.17; H, 3.87; N, 8.06 found: C, 54.33; H, 3.69; N, 7.94.

Ir3': isolated yield 67 mg (59 %).^{1}H NMR (500 MHz, DMSO-*d*$_6$) *δ* 15.43 (s, 1H, N*H*)), 10.49 (s, 2H), 9.24 (s, 1H), 8.69 (d, 2H), 8.15 (s, 3H), 7.78 (d, 2H), 7.77 (m, 2H), 7.68 (d, 2H), 7.63 (t, 2H), 7.06 (d, 2H), 6.71 (s, 2H), 6.67 (d, 2H), 5.93 (s, 2H), 4.03 (t, 2H, O*CH*$_2$), 3.66 (s, 6H, O*CH*$_3$), 1.81 (m, 2H, OCH_2*CH*$_2$), 1.54 (m, 2H, *CH*$_2$$CH_3$), 0.99 (t, 3H, *CH*$_3$).^{13}C NMR (126 MHz, DMSO-*d*$_6$) *δ* 167.22, 160.98, 160.63, 153.28, 149.36, 138.83, 137.34, 128.87 (*C*—N), 127.20, 122.95, 122.25 (*C*-NH), 119.57, 117.22, 115.05, 107.64, 67.79 (O*C*H_2), 54.93 (O*C*H_3), 31.15 (OCH_2*C*H_2), 19.21 (*C*H_2CH_3), 14.18 (CH_2*C*H_3). ^{31}P NMR (202 MHz, DMSO-*d*$_6$): δ −154.74—151.23, 147.72, −144.20, −140.68, −137.17, −133.69. ESI-MS (*m/z*): calcd for $C_{47}H_{40}IrN_6O_3$ 929.2791, found: 929.2904 $[M{-}PF_6]^+$. Elemental analysis: calcd for $C_{47}H_{40}IrN_6O_3PF_6$: C, 52.56; H, 3.75; N, 7.82. found: C, 52.83; H, 3.57; N, 7.64.

Ir4': isolated yield 58 mg (51 %).^{1}H NMR (500 MHz, DMSO-*d*$_6$) *δ* 14.73 (s, 1H, N*H*)), 9.52 (s, 1H), 9.21 (s, 1H), 8.36 (d, 2H), 8.31 (d, 2H), 8.22 (s, 3H), 8.21 (m, 3H), 7.99 (t, 2H), 7.58 (d, 2H), 7.18 (d, 2H), 7.12 (m, 4H), 5.73 (m, 2H), 4.10 (t, 2H, O*CH*$_2$), 1.80 (m, 2H, OCH_2*CH*$_2$), 1.48 (m, 2H, *CH*$_2$$CH_3$), 0.97 (t, 3H, *CH*$_3$). ^{13}C NMR (126 MHz, DMSO-*d*$_6$) *δ* 163.30, 162.28, 160.74, 160.17, 155.13, 153.45, 150.45, 140.37, 128.92 (*C*—N), 128.32, 124.96, 123.74, 122.21 (*C*-NH), 115.15, 113.87, 99.52, 67.84 (O*C*H_2), 31.41 (OCH_2*C*H_2), 22.51 (*C*H_2CH_3), 14.40 (CH_2*C*H_3). ^{31}P NMR (202 MHz, DMSO-*d*$_6$): δ −151.21. −147.70, −144.19, −140.67, −137.16. ^{19}F NMR (471 MHz, DMSO-*d*$_6$): δ −69.41

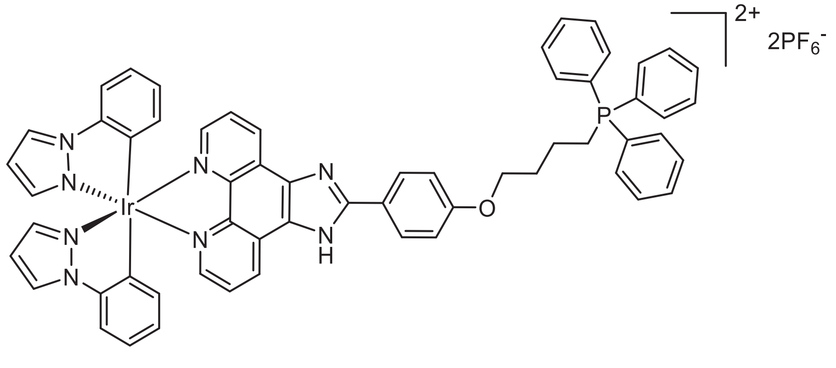

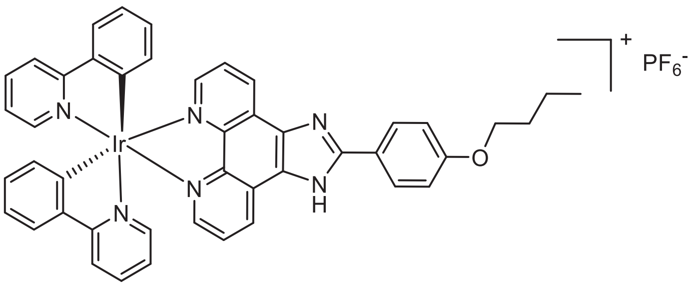

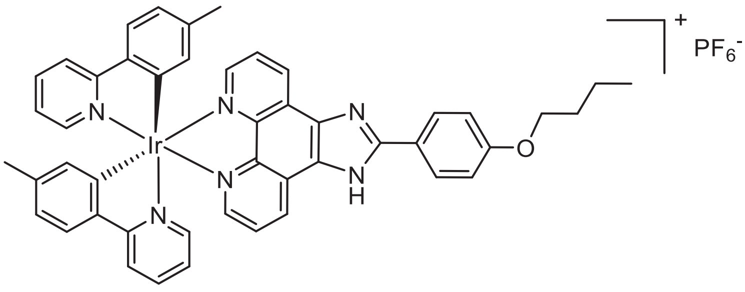

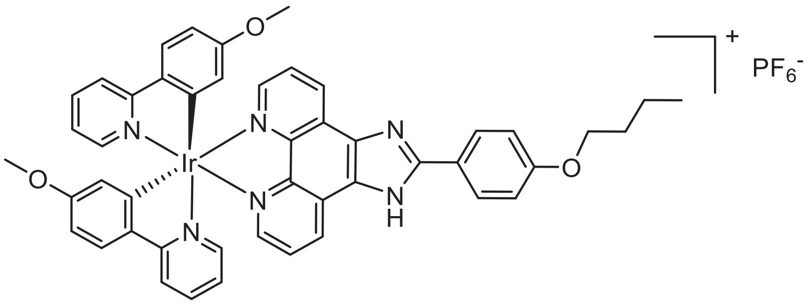

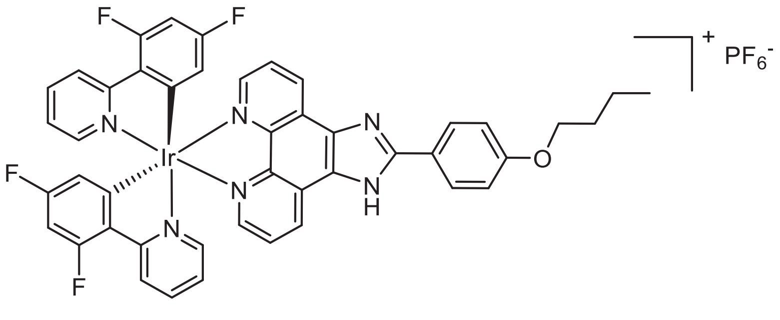

(s), −70.92 (s), −106.60 (d), −108.81 (d). ESI-MS (*m/z*): calcd for $C_{45}H_{32}IrN_6OF_4$ 941.2203 found: 941.2394 $[M-PF_6]^+$. Elemental analysis: calcd for $C_{45}H_{32}IrN_6OPF_{10}$: C, 51.48; H, 3.26; N, 8.00. found: C, 51.63; H, 3.07; N, 7.71.

Ir5': isolated yield 56 mg (55 %). ^{1}H NMR (500 MHz, DMSO-d_6) δ 8.87 (d , 2H), 8.33 (d, 2H), 8.27 (s, 2H), 8.05 (m, 2H), 7.73 (d, 2H), 7.18 (d, 3H), 7.13 (m, 4H), 6.90 (t, 2H), 6.60 (t, 2H), 6.30 (d, 2H), 4.09 (t, 2H, OCH_2), 1.75 (m, 2H OCH_2CH_2), 1.48 (m, 2H, CH_2CH_3), 0.97 (t, 3H, CH_3). ^{13}C NMR (126 MHz, DMSO-d_6) δ 143.65, 139.48, 133.53, 133.01, 129.37 (*C*—N), 128.99, 126.84, 123.49 (*C*-NH), 115.28, 112.58, 108.88, 67.86 (O*C*H$_2$), 31.16 (OCH$_2$*C*H$_2$), 19.21 (*C*H$_2$CH$_3$), 14.19 (CH$_2$*C*H$_3$). ^{31}P NMR (202 MHz, DMSO-d_6): δ −151.22, −147.71, −144.19, −140.68, −137.13. ESI-MS (*m/z*): calcd for $C_{41}H_{34}IrN_8O$ 847.2485 found:847.2476 $[M-PF_6]^+$. Elemental analysis: calcd for $C_{41}H_{34}IrN_8OPF_6$: C, 49.64; H, 3.45; N, 11.30. found: C, 49.83; H, 3.67; N, 11.41.

CRediT authorship contribution statement

Hanxiu Fu: Writing – original draft, Investigation, Formal analysis. **Shuli Wang:** Investigation. **Yuwen Gong:** Investigation. **Heqian Dong:** Investigation. **Kangning Lai:** Investigation. **Zhihao Yang:** Investigation. **Chunyan Fan:** Investigation. **Zhe Liu:** Supervision, Funding

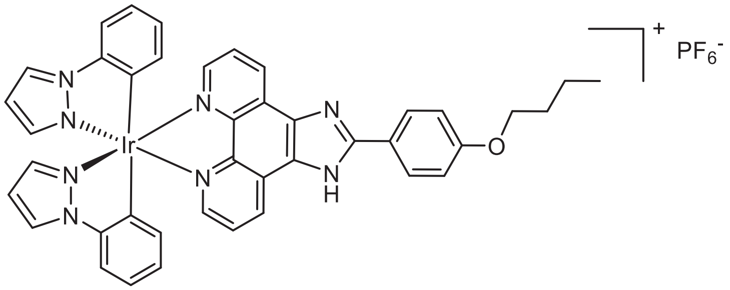

acquisition. **Lihua Guo:** Writing – review & editing, Supervision, Project administration, Conceptualization.

Declaration of competing interest

The authors declare that they have no known competing financial interests or personal relationships that could have appeared to influence the work reported in this paper.

Acknowledgments

We gratefully acknowledge the support from the Taishan Scholars Program, the Natural Science Foundation of Shandong Province (ZR2022MB038), and the Young Talents Invitation Program of Shandong Provincial Colleges and Universities. We also thank Shiyanjia Lab (www.shiyanjia.com) for assisting with the single-crystal XRD data analysis.

Appendix A. Supplementary data

Supplementary materials includes detailed experimental procedures, Figures S1–S69, and Tables S1–S7. Crystallographic data for **Ir4'** (CCDC 2384027) are provided as supplementary material. The CIF and checkCIF files for **Ir4'** are available for free download from the Cambridge Crystallographic Data Centre via www.ccdc.cam.ac.uk/data_request/cif. Supplementary data to this article can be found online at https://doi.org/10.1016/j.bioorg.2025.108148.

Data availability

Data will be made available on request.

References

[1] X. Meng, Y. Yang, L. Zhou, L. Zhang, Y. Lv, S. Li, Y. Wu, M. Zheng, W. Li, G. Gao, G. Deng, T. Jiang, D. Ni, P. Gong, L. Cai, Dual-responsive molecular probe for tumor targeted imaging and photodynamic therapy, Theranostics 7 (2017) 1781–1794, https://doi.org/10.7150/thno.18437.

[2] Z. Lv, H. Wei, Q. Li, X. Su, S. Liu, K.Y. Zhang, W. Lv, Q. Zhao, X. Li, W. Huang, Achieving efficient photodynamic therapy under both normoxia and hypoxia using cyclometalated Ru(II) photosensitizer through type I photochemical process, Chem. Sci. 9 (2018) 502–512, https://doi.org/10.1039/c7sc03765a.

[3] D. Wang, S.J. Lippard, Cellular processing of platinum anticancer drugs, Nat. Rev. Drug. Discov. 4 (2005) 307–320, https://doi.org/10.1038/nrd1691.

[4] L. Kelland, The resurgence of platinum-based cancer chemotherapy, Nat. Rev. Cancer. 7 (2007) 573–584, https://doi.org/10.1038/nrc2167.

[5] T.C. Johnstone, K. Suntharalingam, S.J. Lippard, The next generation of platinum drugs: targeted Pt(II) agents, nanoparticle delivery, and Pt(IV) prodrugs, Chem Rev. 116 (2016) 3436–3486, https://doi.org/10.1021/acs.chemrev.5b00597.

[6] Y. Li, C.P. Tan, W. Zhang, L. He, L.N. Ji, Z.W. Mao, Phosphorescent iridium(III)-bis-N-heterocyclic carbene complexes as mitochondria-targeted theranostic and photodynamic anticancer agents, Biomaterials 39 (2015) 95–104, https://doi.org/10.1016/j.biomaterials.2014.10.070.

[7] E.K. Lim, T. Kim, S. Paik, S. Haam, Y.M. Huh, K. Lee, Nanomaterials for theranostics: recent advances and future challenges, Chem. Rev. 115 (2015) 327–394, https://doi.org/10.1021/cr300213b.

[8] A. Zamora, G. Vigueras, V. Rodríguez, M.D. Santana, J. Ruiz, Cyclometalated iridium(III) luminescent complexes in therapy and phototherapy, Coord. Chem. Rev. 360 (2018) 34–76, https://doi.org/10.1016/j.ccr.2018.01.010.

[9] C.P. Tan, Y.M. Zhong, L.N. Ji, Z.W. Mao, Phosphorescent metal complexes as theranostic anticancer agents: combining imaging and therapy in a single molecule, Chem. Sci. 12 (2021) 2357–2367, https://doi.org/10.1039/d0sc06885.

[10] L. Filippi, A. Chiaravalloti, O. Schillaci, R. Cianni, O. Bagni, Theranostic approaches in nuclear medicine: current status and future prospects, Expert. Rev. Med. Devices 17 (2020) 331–343, https://doi.org/10.1080/17434440.2020.1741348.

[11] H. Chen, W. Zhang, G. Zhu, J. Xie, X. Chen, Rethinking cancer nanotheranostics, Nat. Rev. Mater. 2 (2017) 17024, https://doi.org/10.1038/natrevmats.2017.24.

[12] X.D. Zhang, J. Chen, Y. Min, G.B. Park, X. Shen, S.S. Song, Y.M. Sun, H. Wang, W. Long, J. Xie, K. Gao, L. Zhang, S. Fan, F. Fan, U. Jeong, Metabolizable Bi_2Se_3 nanoplates: biodistribution, toxicity, and uses for cancer radiation therapy and imaging, Adv. Funct. Mater. 24 (2014) 1718–1729, https://doi.org/10.1002/adfm.201302312.

[13] Z. Liu, P.J. Sadler, Organoiridium complexes: anticancer agents and catalysts, Acc. Chem. Res. 47 (2014) 1174–1185, https://doi.org/10.1021/ar400266c.

[14] D.L. Ma, C. Wu, K.J. Wu, C.H. Leung, Iridium(III) complexes targeting apoptotic cell death in cancer cells, Molecules 24 (2019) 2739, https://doi.org/10.3390/molecules24152739.

[15] L.C. Lee, K.K. Leung, K.K. Lo, Recent development of luminescent rhenium(I) tricarbonyl polypyridine complexes as cellular imaging reagents, anticancer drugs, and antibacterial agents, Dalton. Trans. 46 (2017) 16357–16380, https://doi.org/10.1039/C7DT03465B.

[16] J.J. Cao, C.P. Tan, M.H. Chen, N. Wu, D.Y. Yao, X.G. Liu, L.N. Ji, Z.W. Mao, Targeting cancer cell metabolism with mitochondria-immobilized phosphorescent cyclometalated iridium(III) complexes, Chem. Sci. 8 (2017) 631–640, https://doi.org/10.1039/C6SC02901A.

[17] W. Lv, Z. Zhang, K.Y. Zhang, H. Yang, S. Liu, A. Xu, S. Guo, Q. Zhao, W. Huang, A mitochondria-targeted photosensitizer showing improved photodynamic therapy effects under hypoxia, Angew. Chem. Int. Ed. Engl. 55 (2016) 9947–9951, https://doi.org/10.1002/anie.201604130.

[18] Y. Chen, T.W. Rees, L. Ji, H. Chao, Mitochondrial dynamics tracking with iridium (III) complexes, Curr. Opin. Chem. Biol. 43 (2018) 51–57, https://doi.org/10.1016/j.cbpa.2017.11.006.

[19] X.W. Wu, Y. Zheng, F.X. Wang, J.J. Cao, H. Zhang, D.Y. Zhang, C.P. Tan, L.N. Ji, Z. W. Mao, Anticancer Ir(III)–aspirin conjugates for enhanced metabolic immunomodulation and mitochondrial lifetime imaging, Chem. Eur. J. 25 (2019) 7012–7022, https://doi.org/10.1002/chem.201900851.

[20] S. Mukhopadhyay, R.K. Gupta, R.P. Paitandi, N.K. Rana, G. Sharma, B. Koch, L. K. Rana, M.S. Hundal, D.S. Pandey, Synthesis, structure, DNA/protein binding, and anticancer activity of some half-sandwich cyclometalated Rh(III) and Ir(III) complexes, Organometallics 34 (2015) 4491–4506, https://doi.org/10.1021/acs.organomet.5b00475.

[21] L. Hao, Z.W. Li, D.Y. Zhang, L. He, W. Liu, J. Yang, C.P. Tan, L.N. Ji, Z.W. Mao, Monitoring mitochondrial viscosity with anticancer phosphorescent Ir(III) complexes via two-photon lifetime imaging, Chem. Sci. 10 (2019) 1285–1293, https://doi.org/10.1039/C8SC04242J.

[22] S. Liu, N. Zhou, Z. Chen, H. Wei, Y. Zhu, S. Guo, Q. Zhao, Using a redox-sensitive phosphorescent probe for optical evaluation of an intracellular redox environment, Opt. Lett. 42 (2017) 13–16, https://doi.org/10.1364/OL.42.000013.

[23] M. Wang, Z. Mao, T.S. Kang, C.Y. Wong, J.L. Mergny, C.H. Leung, D.L. Ma, Conjugating a groove-binding motif to an Ir(III) complex for the enhancement of G-quadruplex probe behavior, Chem. Sci. 7 (2016) 2516–2523, https://doi.org/10.1039/c6sc00001k.

[24] L.C. Lee, J.C. Lau, H.W. Liu, K.K. Lo, Conferring phosphorogenic properties on iridium(III)-based bioorthogonal probes through modification with a nitrone unit, Angew. Chem. Int. Ed. Engl. 55 (2016) 1046–1049, https://doi.org/10.1002/anie.201509396.

[25] H.K. Saeed, S. Sreedharan, P.J. Jarman, S.A. Archer, S.D. Fairbanks, S.P. Foxon, A. J. Auty, D. Chekulaev, T. Keane, A. Meijer, J.A. Weinstein, C.G.W. Smythe, J. Bernardino de la Serna, J.A. Thomas, Making the right link to theranostics: the photophysical and biological properties of dinuclear Ru(II)-Re(I) dppz complexes depend on their tether, J. Am. Chem. Soc. 142 (2020) 1101–1111, https://doi.org/10.1021/jacs.9b12564.

[26] K.K. Lo, Molecular design of bioorthogonal probes and imaging reagents derived from photofunctional transition metal complexes, Acc. Chem. Res. 53 (2020) 32–44, https://doi.org/10.1021/acs.accounts.9b00416.

[27] L. He, C.P. Tan, R.R. Ye, Y.Z. Zhao, Y.H. Liu, Q. Zhao, L.N. Ji, Z.W. Mao, Theranostic iridium(III) complexes as one and two-photon phosphorescent trackers to monitor autophagic lysosomes, Angew. Chem. Int. Ed. Engl. 53 (2014) 12137–12141, https://doi.org/10.1002/anie.201407468.

[28] R. Kumar, W.S. Shin, K. Sunwoo, W.Y. Kim, S. Koo, S. Bhuniya, J.S. Kim, Small conjugate-based theranostic agents: an encouraging approach for cancer therapy, Chem. Soc. Rev. 44 (2015) 6670–6683, https://doi.org/10.1039/c5cs00224a.

[29] R.R. Ye, C.P. Tan, L.N. Ji, Z.W. Mao, Coumarin-appended phosphorescent cyclometalated iridium(III) complexes as mitochondria-targeted theranostic anticancer agents, Dalton. Trans. 45 (2016) 13042–13051, https://doi.org/10.1039/c6dt00601a.

[30] P.E. Porporato, N. Filigheddu, J.M.B. Pedro, G. Kroemer, L. Galluzzi, Mitochondrial metabolism and cancer, Cell Res. 28 (2018) 265–280, https://doi.org/10.1038/cr.2017.155.

[31] L.D. Zorova, V.A. Popkov, E.Y. Plotnikov, D.N. Silachev, I.B. Pevzner, S. S. Jankauskas, V.A. Babenko, S.D. Zorov, A.V. Balakireva, M. Juhaszova, S. J. Sollott, D.B. Zorov, Mitochondrial membrane potential, Anal. Biochem. 552 (2018) 50–59, https://doi.org/10.1016/j.ab.2017.07.009.

[32] P. Mishra, D.C. Chan, Mitochondrial dynamics and inheritance during cell division, development and disease, Nat. Rev. Mol. Cell Biol. 15 (2014) 634–646, https://doi.org/10.1038/nrm3877.

[33] G.L. Indig, G.S. Anderson, M.G. Nichols, J.A. Bartlett, W.S. Mellon, F. Sieber, Effect of molecular structure on the performance of triarylmethane dyes as therapeutic agents for photochemical purging of autologous bone marrow grafts from residual tumor cells, J. Pharm. Sci. 89 (2000) 88–99, https://doi.org/10.1002/(SICI)1520-6017(200001)89:1<88::AID-JPS9>3.0.CO;2-K.

[34] Q. Li, Y. Huang, Mitochondrial targeted strategies and theirapplication for cancer and other diseases treatment, J. Pharm. Invest. 50 (2020) 271–293, https://doi.org/10.1007/s40005-020-00481-0.

[35] D.A. Safin, M.P. Mitoraj, K. Robeyns, Y. Filinchuk, C.M. Vande Velde, Luminescent mononuclear mixed ligand complexes of copper(I) with 5-phenyl-2,2`-bipyridine and triphenylphosphine, Dalton Trans. 44 (2015) 16824–16832, https://doi.org/10.1039/c5dt02755a.

[36] M.F. Ross, G.F. Kelso, F.H. Blaikie, A.M. James, H.M. Cochemé, A. Filipovska, T. Da Ros, T.R. Hurd, R.A. Smith, M.P. Murphy, Lipophilic triphenylphosphonium cations as tools in mitochondrial bioenergetics and free radical biology, Biochemistry (Mosc.) 70 (2005) 222–230, https://doi.org/10.1007/s10541-005-0104-5.

[37] E.A. Liberman, V.P. Topaly, L.M. Tsofina, A.A. Jasaitis, V.P. Skulachev, Mechanism of coupling of oxidative phosphorylation and the membrane potential of mitochondria, Nature 222 (1969) 1076–1078, https://doi.org/10.1038/2221076a0.

[38] M.P. Murphy, Selective targeting of bioactive compounds to mitochondria, Trends Biotechnol. 15 (1997) 326–330, https://doi.org/10.1016/S0167-7799(97)01068-8.

[39] M.P. Murphy, R.A. Smith, Drug delivery to mitochondria: the key to mitochondrial medicine, Adv. Drug. Deliv. Rev. 41 (2000) 235–250, https://doi.org/10.1016/s0169-409x(99)00069-1.

[40] X. Cheng, D. Feng, J. Lv, X. Cui, Y. Wang, Q. Wang, L. Zhang, Application prospects of triphenylphosphine-based mitochondria-targeted cancer therapy, Cancers 15 (2023) 666, https://doi.org/10.3390/cancers15030666.

[41] J. Wang, Y. Song, Z. Huang, W. Lin, G. Yu, Y. Xiong, G. Jiang, Y. Tan, J. Wang, X. Liao, Coupling a virulence-targeting moiety with Ru-based AMP mimics efficiently improved its anti-infective potency and therapeutic index, J. Med. Chem. 66 (2023) 13304–13318, https://doi.org/10.1021/acs.jmedchem.3c01282.

[42] S. Marrache, R.K. Pathak, S. Dhar, Detouring of cisplatin to access mitochondrial genome for overcoming resistance, Proc. Natl. Acad. Sci. U. S. A. 111 (2014) 10444–10449, https://doi.org/10.1073/pnas.1405244111.

[43] Z. Zhu, Z. Wang, C. Zhang, Y. Wang, H. Zhang, Z. Gan, Z. Guo, X. Wang, Mitochondrion-targeted platinum complexes suppressing lung cancer through multiple pathways involving energy metabolism, Chem. Sci. 10 (2019) 3089–3095, https://doi.org/10.1039/c8sc04871a.

[44] P. Li, L. Guo, J. Li, Z. Yang, H. Fu, K. Lai, H. Dong, C. Fan, Z. Liu, Mitochondria-targeted neutral and cationic iridium(III) anticancer complexes chelating simple hybrid sp^2-N/sp^3-N donor ligands, Dalton. Trans. 53 (2024) 1977–1988, https://doi.org/10.1039/d3dt03700b.

[45] X.D. Song, X. Kong, S.F. He, J.X. Chen, J. Sun, B.B. Chen, J.W. Zhao, Z.W. Mao, Cyclometalated iridium(III)-guanidinium complexes as mitochondria-targeted anticancer agents, Eur. J. Med. Chem. 138 (2017) 246–254, https://doi.org/10.1016/j.ejmech.2017.06.038.

[46] P. Selvam, S. De, P. Paira, S.K.A. Kumar, S. Kumar R, A. Moorthy, A. Ghosh, Y.-C. Kuo, S. Banerjee, S.K. Jenifer, In vitro studies on the selective cytotoxic effect of luminescent Ru(II)-p-cymene complexes of imidazo-pyridine and imidazo quinoline ligands, Dalton Trans. 51 (2022) 17263–17276, https://doi.org/10.1039/d2dt02237k.

[47] R.L. Panchangam, R.N. Rao, M.M. Balamurali, T.B. Hingamire, D. Shanmugam, V. Manickam, K. Chanda, Antitumor effects of Ir(III)-2H-indazole complexes for triple negative breast cancer, Inorg. Chem. 60 (2021) 17593–17607, https://doi.org/10.1021/acs.inorgchem.1c02193.

[48] Y. Yang, L. Guo, X. Ge, W. Chen, H. Zhou, T. Zhu, X. Li, S. Tuo, Z. Liu, Fluorescent zwitterionic Iridium(III) complexes containing sulfonate groups: synthesis, biological activity and tracking in live cells, Dyes Pigm. 176 (2020) 108220, https://doi.org/10.1016/j.dyepig.2020.108220.

[49] Y. Yang, L. Guo, X. Ge, Z. Tian, Y. Gong, H. Zheng, Q. Du, X. Zheng, Z. Liu, Novel lysosome-targeted cyclometalated Iridium(III) anticancer complexes containing imine-N-heterocyclic carbene ligands: Synthesis, spectroscopic properties and biological activity, Dyes Pigm. 161 (2019) 119–129, https://doi.org/10.1016/j.dyepig.2018.09.044.

[50] H. Xiang, H. Chen, H.P. Tham, S.Z.F. Phua, J.G. Liu, Y. Zhao, Cyclometalated iridium(III)-complex-based micelles for glutathione-responsive targeted chemotherapy and photodynamic therapy, ACS Appl. Mater. Interfaces 9 (2017) 27553–27562, https://doi.org/10.1021/acsami.7b09506.

[51] J. Li, L. Guo, Z. Tian, M. Tian, S. Zhang, K. Xu, Y. Qian, Z. Liu, Novel half-sandwich iridium(III) imino-pyridyl complexes showing remarkable in vitro anticancer activity, Dalton. Trans. 46 (2017) 15520–15534, https://doi.org/10.1039/c7dt03265j.

[52] A. Petrović, M.M. Milutinović, E.T. Petri, M. Živanović, N. Milivojević, R. Puchta, A. Scheurer, J. Korzekwa, O.R. Klisurić, J. Bogojeski, Synthesis of camphor-derived bis(pyrazolylpyridine) rhodium(III) complexes: structure-reactivity relationships and biological activity, Inorg. Chem. 58 (2019) 307–319, https://doi.org/10.1021/acs.inorgchem.8b02390.

[53] S. Thota, D.A. Rodrigues, D.C. Crans, E.J. Barreiro, Ru(II) compounds: next-generation anticancer metallotherapeutics? J. Med. Chem. 61 (2018) 5805–5821, https://doi.org/10.1021/acs.jmedchem.7b01689.

[54] P. Selvam, S. De, P. Paira, S.K.A. Kumar, R.S. Kumar, A. Moorthy, A. Ghosh, Y. C. Kuo, S. Banerjee, S.K. Jenifer, In vitro studies on the selective cytotoxic effect of luminescent Ru(II)-p-cymene complexes of imidazo-pyridine and imidazo quinoline ligands, Dalton. Trans. 51 (2022) 17263–17276, https://doi.org/10.1039/d2dt02237k.

[55] Y. Yang, L. Guo, Z. Tian, Y. Gong, H. Zheng, S. Zhang, Z. Xu, X. Ge, Z. Liu, Novel and versatile imine-N-heterocyclic carbene half-sandwich iridium(III) complexes as lysosome-targeted anticancer agents, Inorg. Chem. 57 (2018) 11087–11098, https://doi.org/10.1021/acs.inorgchem.8b01656.

[56] J. Ruiz, C. Vicente, C. Haro, D. Bautista, Novel bis-C,N-cyclometalated iridium(III) thiosemicarbazide antitumor complexes: interactions with human serum albumin and DNA, and inhibition of cathepsin B, Inorg. Chem. 52 (2013) 974–982, https://doi.org/10.1021/ic302219v.

[57] F. Samari, B. Hemmateenejad, M. Shamsipur, M. Rashidi, H. Samouei, Affinity of two novel five-coordinated anticancer Pt(II) complexes to human and bovine serum albumins: a spectroscopic approach, Inorg. Chem. 51 (2012) 3454–3464, https://doi.org/10.1021/ic202141g.

[58] W. He, Y. Li, C. Xue, Z. Hu, X. Chen, F. Sheng, Effect of Chinese medicine alpinetin on the structure of human serum albumin, Bioorg. Med. Chem. 13 (2005) 1837–1845, https://doi.org/10.1016/j.bmc.2004.11.038.

[59] C. Li, M. Yu, Y. Sun, Y. Wu, C. Huang, F. Li, A nonemissive iridium(III) complex that specifically lights-up the nuclei of living cells, J. Am. Chem. Soc. 133 (2011) 11231–11239, https://doi.org/10.1021/ja202344c.

[60] C.A. Puckett, J.K. Barton, Mechanism of cellular uptake of a ruthenium polypyridyl complex, Biochemistry 47 (2008) 11711–11716, https://doi.org/10.1021/bi800856t.

[61] M.P. Murphy, Slip and leak in mitochondrial oxidative phosphorylation, Biochim. Biophys. Acta 977 (1989) 123–141, https://doi.org/10.1016/s0005-2728(89)80063-5.

[62] K. Qiu, Y. Chen, T.W. Rees, L. Ji, H. Chao, Organelle-targeting metal complexes: from molecular design to bio-applications, Coord. Chem. Rev. 378 (2019) 66–86, https://doi.org/10.1016/j.ccr.2017.10.022.

[63] J. Li, M. Tian, Z. Tian, S. Zhang, C. Yan, C. Shao, Z. Liu, Half-sandwich iridium(III) and ruthenium(II) complexes containing P^P-chelating ligands: a new class of potent anticancer agents with unusual redox features, Inorg. Chem. 57 (2018) 1705–1716, https://doi.org/10.1021/acs.inorgchem.7b01959.

[64] A. Arunachalam, R. Rengan, D. Umapathy, A.J.V. Arockiam, Impact of biphenyl benzhydrazone-incorporated arene Ru(II) complexes on cytotoxicity and the cancer cell death mechanism, Organometallics 41 (2018) 2474–2486, https://doi.org/10.1021/acs.organomet.2c00290.

[65] A.C. Carrasco, V. Rodríguez-Fanjul, A. Habtemariam, A.M. Pizarro, Structurally strained half-sandwich iridium(III) complexes as highly potent anticancer agents, J. Med. Chem. 63 (2020) 4005–4021, https://doi.org/10.1021/acs.jmedchem.9b02000.

[66] I. Echevarría, E. Zafon, S. Barrabés, M.Á. Martínez, S. Ramos-Gómez, N. Ortega, B. R. Manzano, F.A. Jalón, R. Quesada, G. Espino, A. Massaguer, Rational design of mitochondria targeted thiabendazole-based Ir(III) biscyclometalated complexes for a multimodal photodynamic therapy of cancer, J. Inorg. Biochem. 231 (2022) 111790, https://doi.org/10.1016/j.jinorgbio.2022.111790.

[67] J.M. Gichumbi, H.B. Friedrich, Half-sandwich complexes of platinum group metals (Ir, Rh, Ru and Os) and some recent biological and catalytic applications, J. Organomet. Chem. 866 (2018) 123–143, https://doi.org/10.1016/j.jorganchem.2018.04.02.

[68] S. Swaminathan, R.J. Deepak, R. Karvembu, Interweaving catalysis and cancer using Ru- and Os-arene complexes to alter cellular redox state: a structure-activity relationship (SAR) review, Coord. Chem. Rev. 491 (2023) 215230, https://doi.org/10.1016/j.ccr.2023.215230.

[69] I. Romero-Canelón, M. Mos, P.J. Sadler, Enhancement of selectivity of an organometallic anticancer agent by redox modulation, J. Med. Chem. 58 (2015) 7874–7880, https://doi.org/10.1021/acs.jmedchem.5b00655.

[70] I. Romero-Canelón, P.J. Sadler, Next-generation metal anticancer complexes: multitargeting via redox modulation, Inorg. Chem. 52 (2013) 12276–12291, https://doi.org/10.1021/ic400835n.

[71] I.E. Scheffler, A century of mitochondrial research: achievements and perspectives, Mitochondrion 1 (2001) 3–31, https://doi.org/10.1016/s1567-7249(00)00002-7.

[72] J. Dan Dunn, L.A. Alvarez, X. Zhang, T. Soldati, Reactive oxygen species and mitochondria: A nexus of cellular homeostasis, Redox Biol. 6 (2015) 472–485, https://doi.org/10.1016/j.redox.2015.09.005.

[73] Y. Ye, T. Zhang, H. Yuan, D. Li, H. Lou, P. Fan, Mitochondria-targeted lupane triterpenoid derivatives and their selective apoptosis-inducing anticancer mechanisms, J. Med. Chem. 60 (2017) 6353–6363, https://doi.org/10.1021/acs.jmedchem.7b00679.

[74] N. Popgeorgiev, J.D. Sa, L. Jabbour, S. Banjara, T.T.M. Nguyen, A. Akhavan-E-Sabet, R. Gadet, N. Ralchev, S. Manon, M.G. Hinds, H.-J. Osigus, B. Schierwater, P. O. Humbert, R. Rimokh, G. Gillet, M. Kvansakul, Ancient and conserved functional interplay between bcl-2 family proteins in the mitochondrial pathway of apoptosis, Sci. Adv. 6 (2020) eabc4149, https://doi.org/10.1126/sciadv.abc4149.

[75] B. Song, J. Li, J. Li, Pomegranate peel extract polyphenols induced apoptosis in human hepatoma cells by mitochondrial pathway, Food Chem. Toxicol. (2016) 158–166, https://doi.org/10.1016/j.fct.2016.04.020.

[76] S. Kozieł, U.K. Komarnicka, A. Ziółkowska, A. Skórska-Stania, B. Pucelik, M. Płotek, V. Sebastian, A. Bieńko, G. Stochel, A. Kyzioł, Anticancer potency of novel organometallic Ir(III) complexes with phosphine derivatives of fluoroquinolones encapsulated in polymeric micelles, Inorg. Chem. Front. 7 (2020) 3386–3401, https://doi.org/10.1039/D0QI00538J.

[77] P. Friedl, S. Alexander, Cancer invasion and the microenvironment: plasticity and reciprocity, Cell 147 (2011) 992–1009, https://doi.org/10.1016/j.cell.2011.11.016.

[78] S. Valastyan, R.A. Weinberg, Tumor metastasis: molecular insights and evolving paradigms, Cell 147 (2011) 275–292, https://doi.org/10.1016/j.cell.2011.09.024.

[79] S. Patil, S. Pandey, A. Singh, M. Radhakrishna, S. Basu, Hydrazide-hydrazone small molecules as AIEgens: illuminating mitochondria in cancer cells, Chem 25 (2019) 8229–8235, https://doi.org/10.1002/chem.201901074.

[80] B.B. Chen, N.L. Pan, J.X. Liao, M.Y. Huang, D.C. Jiang, J.J. Wang, H.J. Qiu, J. X. Chen, L. Li, J. Sun, Cyclometalated iridium(III) complexes as mitochondria-targeted anticancer and antibacterial agents to induce both autophagy and apoptosis, J. Inorg. Biochem. 219 (2021) 111450, https://doi.org/10.1016/j.jinorgbio.2021.111450.